



# Evolution of oxygen and stratification and their relationship in the North Pacific Ocean in CMIP6 Earth system models

Lyuba Novi<sup>1</sup>, Annalisa Bracco<sup>1</sup>, Takamitsu Ito<sup>1</sup>, and Yohei Takano<sup>2,3</sup>

<sup>1</sup>School of Earth and Atmospheric Sciences, Georgia Institute of Technology, Atlanta, GA, USA

<sup>2</sup>British Antarctic Survey, Cambridge, UK

<sup>3</sup>Los Alamos National Laboratory, Los Alamos, NM, USA

**Correspondence:** Lyuba Novi (lnovi3@gatech.edu)

Received: 7 August 2023 – Discussion started: 7 September 2023

Revised: 17 April 2024 – Accepted: 30 May 2024 – Published: 13 September 2024

**Abstract.** This study examines the linkages between the upper-ocean (0–200 m) oxygen ( $O_2$ ) content and stratification in the North Pacific Ocean using four Earth system models (ESMs), an ocean hindcast simulation, and an ocean reanalysis. The trends and variability in oceanic  $O_2$  content are driven by the imbalance between physical supply and biological demand. Physical supply is primarily controlled by ocean ventilation, which is responsible for the transport of  $O_2$ -rich surface waters to the subsurface. Isopycnic potential vorticity (IPV), a quasi-conservative tracer proportional to density stratification that can be evaluated from temperature and salinity measurements, is used herein as a dynamical proxy for ocean ventilation. The predictability potential of the IPV field is evaluated through its information entropy. The results highlight a strong  $O_2$ –IPV connection and somewhat higher (as compared to the rest of the basin) predictability potential for IPV across the tropical Pacific, where the El Niño–Southern Oscillation occurs. This pattern of higher predictability and strong anticorrelation between  $O_2$  and stratification is robust across multiple models and datasets. In contrast, IPV at mid-latitudes has low predictability potential and its center of action differs from that of  $O_2$ . In addition, the locations of extreme events or hotspots may or may not differ between the two fields, with a strong model dependency, which persists in future projections. On the one hand, these results suggest that it may be possible to monitor ocean  $O_2$  in the tropical Pacific based on a few observational sites co-located with the more abundant IPV measurements; on the other, they lead us to question the robustness of the IPV– $O_2$  relationship in the extratropics. The proposed framework helps to characterize and interpret  $O_2$

variability in relation to physical variability and may be especially useful in the analysis of new observation-based data products derived from the BGC-Argo float array in combination with the traditional but far more abundant Argo data.

## 1 Introduction

Dissolved oxygen ( $O_2$ ) in the oceans is crucial for biogeochemical cycling, marine ecosystems, and the redox chemistry of seawater.  $O_2$  is a key element for the survival and functioning of marine organisms, as fish, shellfish, marine mammals, and other aquatic life rely on  $O_2$  to breathe and carry out essential metabolic processes. Growth, reproduction, and the overall health of marine organisms depend on the balance between metabolic demands and  $O_2$  supply (Deutsch et al., 2015).

Ocean deoxygenation refers to the long-term decrease in the concentration of  $O_2$  in the Earth's oceans. At the global scale, according to historical observations, the  $O_2$  inventory has been declining significantly during the past decades (Ito et al., 2017; Schmidtko et al., 2017). Changes in  $O_2$  concentrations can reflect the impacts of climate change, nutrient pollution, eutrophication, and other human-induced stressors (e.g., Breitburg et al., 2018). Predicting  $O_2$  levels in the oceans is especially important around and within oxygen minimum zones (OMZs), which are characterized by layers in the water column with very low  $O_2$  concentration due to biological, chemical, and physical processes. As oceans warm, OMZs are posed to increase in number and size across the globe, thereby threatening marine ecosys-

tems. In the North Pacific, a large OMZ exists on the eastern side of the tropical Pacific, and its variability and trends are important for nitrogen cycling and the production of N<sub>2</sub>O, a potent greenhouse gas (Nevison et al., 2003; Yang et al., 2017). However, O<sub>2</sub> measurements are temporally and spatially sparse, and trends remain uncertain: the decline in O<sub>2</sub> between 1970 and 2010 is estimated to be around  $-0.48 \pm 0.35$  % per decade in the upper 1000 m (Bindoff et al., 2019). The uncertainty in ocean deoxygenation estimates is due to different interpolation methods, data quality control standards, and data sources, the latter varying from shipboard measurements (ship-based bottle measurements and CTD–O<sub>2</sub> profiles) to biogeochemical Argo floats (Roemmich et al., 2019).

Interpreting changes in O<sub>2</sub> concentrations requires an understanding of how ocean circulation, mixing, air–sea gas exchange, biological productivity, and respiration operate. The air–sea gas exchange for O<sub>2</sub> is relatively efficient, and it maintains the surface water close to saturation with the overlying atmosphere for ice-free regions. Ocean circulation is the primary pathway through which O<sub>2</sub> is supplied (or ventilated) into the thermocline and deep ocean. At the subsurface, O<sub>2</sub> is gradually consumed by respiration due to the decomposition of dissolved and particulate organic matter. The O<sub>2</sub> concentration progressively decreases as water masses age. At the climatological timescale, the rates of O<sub>2</sub> supply and consumption are balanced to sustain a steady state. In another words, changes in O<sub>2</sub> concentration are caused by an imbalance between O<sub>2</sub> supply and O<sub>2</sub> consumption. On the supply side, the ventilation of O<sub>2</sub> is essentially controlled by ocean circulation and mixing processes. Broadly, ventilation refers to the exchange of water between the surface layer and the ocean’s interior (Talley et al., 2011) and involves a wide range of physical processes such as the wind-driven shallow overturning associated with subtropical cells (Brandt et al., 2015; Duteil et al., 2014; Eddebbar et al., 2019), the formation of mode and intermediate waters (Claret et al., 2018; Sallée et al., 2010, 2012; Gnanadesikan et al., 2012), and lateral (isopycnal) eddy stirring (Rudnickas et al., 2019; Gnanadesikan et al., 2013, 2015). These circulation systems are ultimately driven by atmospheric winds and air–sea buoyancy fluxes, which exhibit significant interannual, decadal, and multi-decadal variability. Fluctuations in ventilation rates as well as in ocean stratification are known to impact both O<sub>2</sub> levels (Ridder and England, 2014; Duteil et al., 2014; McKinley et al., 2004) and the distribution of isopycnal potential vorticity (IPV), a dynamical tracer which is proportional to the local stratification and the Coriolis parameter. Use of the absolute value of the Coriolis parameter in the formula, as indicated by \*, guarantees that the relationship with stratification holds with the same sign in both hemispheres, so a higher IPV\* indicates stronger stratification and vice versa. A strong wintertime convective mixing will produce weakly stratified O<sub>2</sub>-rich water masses (low IPV\* and high O<sub>2</sub>) and vice versa. These properties are then brought

together into the ocean’s interior following the pathway of large-scale ocean currents.

In this study, we build upon this relationship and explore the overarching hypothesis that IPV\* may be used as a proxy for O<sub>2</sub> with a focus on the North Pacific basin. If this is the case, then IPV\* may provide a means to monitor and predict the evolution of O<sub>2</sub>. In the North Pacific, the Pacific Decadal Oscillation (PDO) is the mode of climate variability that exerts the greatest control on stratification and O<sub>2</sub>, as shown by Ito et al. (2019). Indeed, the dominant mode of oxygen variability in the North Pacific Ocean is correlated with the PDO index such that the PDO explains about 25 % of its variance. In the tropics, the PDO modulates the depths of isopycnal surfaces and biological productivity and respiration together with the El Niño–Southern Oscillation (ENSO), while at mid-latitudes it is the dominant mode influencing the depth of winter-mixed-layer ventilation and ventilation processes. Here we analyze outputs from the Coupled Model Intercomparison Project Phase 6 (CMIP6; Eyring et al., 2016), a major international effort with the primary objective of providing a standardized framework for simulating past, present, and future climate conditions. The participating modeling groups run their climate models under prescribed forcing fields and following a common protocol, thereby generating a comprehensive set of output datasets which are freely available to the scientific community through data portals and archives provided by the Earth System Grid Federation (ESGF). Using a suite of Earth system models (ESMs) run with prescribed carbon dioxide concentrations, we address the following questions:

- How robust is the relationship between O<sub>2</sub> and IPV\* in the North Pacific across several ESMs and how may it evolve by the end of the 21st century (related to HYP 1; see below)?
- What are the linkages between O<sub>2</sub> and IPV\* and large-scale modes of climate variability such as PDO and ENSO (related to HYP 2)?
- Where are the hotspots of changes in IPV\* and O<sub>2</sub> in the historical period and in the projections, and are they co-located or do they differ in space and time (related to HYP 3)?

Our specific objectives are to evaluate the hypotheses that ocean ventilation (IPV\*) regulates O<sub>2</sub> variability in the North Pacific (HYP 1); that the PDO/ENSO–ventilation–O<sub>2</sub> linkage provides the basis for the predictability of O<sub>2</sub> whenever IPV\* is predictable (HYP 2); and that the linkage can be exploited to identify hotspots of changes in O<sub>2</sub> variability, means, and extremes (HYP 3; see “Materials and methods”). While testing these hypotheses, we also aim to introduce recently developed approaches for model intercomparison and data analysis to the ocean biogeochemistry community. Specifically, in this work we adopt the information

entropy (IE; Prado et al., 2020) concept for evaluating predictability, a data-mining tool for dimensionality reduction and network analysis ( $\delta$ -MAPS; Fountalis et al., 2018), and the standard Euclidean distance (SED) index (Diffenbaugh and Giorgi, 2012) to evaluate changes in the fields we analyze. In short, IE is a metric that measures the amount of randomness and therefore unpredictability in a dataset. For example, if a time series is a random sequence, its entropy will be high, while if a time series follows a sinusoidal curve, its IE will be low. On the other hand,  $\delta$ -MAPS combines feature extraction and network analysis into a single framework. Its goal is to identify key features and to visualize how those features relate to one another. Finally, the SED index is a simple and flexible method used to detect *total* changes in one or more variables in a given dataset (in other words, to identify regions that stand out for changes in means, extremes, and variability) through measuring the distance in multi-variate space between a baseline period and any other. After introducing these tools in more detail in Sect. 2, a description of the data analyzed in this work follows in Sect. 3. Results are then presented in Sect. 4, with a general discussion and conclusions to close.

## 2 Materials and methods

In this section, we describe the three tools recently developed for climate science applications and adopted in our analysis as well as how we calculate IPV\*. The information entropy (IE) is used to evaluate predictability. IE is defined following Prado et al. (2020) and is based on the recurrence of microstates in a recurrence plot (RP). An RP (Eckmann et al., 1987) is a visualization technique for trajectory recurrence of a given dynamical system described in phase space by a matrix  $\mathbf{R}_{ij}$  such that

$$\mathbf{R}_{ij}(\epsilon) = \Theta(\epsilon - \|\mathbf{x}_i - \mathbf{x}_j\|), \mathbf{x}_i \in \mathbb{R}^d, i, j = 1, 2, \dots, K, \quad (1)$$

where  $\Theta$  is the Heaviside function;  $\|\cdot\|$  is an Euclidean distance;  $\mathbf{x}_i$  and  $\mathbf{x}_j$  are, in our work, states at time steps  $i$  and  $j$ ;  $\epsilon$  is a threshold distance (the maximum distance between two states to be considered mutually recurrent);  $d$  is the  $\mathbf{x}_i$  space dimension; and  $K$  is the number of states considered (the length of each analyzed time series).  $\mathbf{R}_{ij}$  is a matrix that represents non-recurrent (as zeros) and recurrent (as ones) states in phase space, and it is explicitly dependent on  $\epsilon$ . Corso et al. (2018) introduced the *recurrence entropy* quantifier, for which for a given time series, the probability of occurrence of microstates in its RP is quantified without the need for a space-state reconstruction. A microstate of dimension  $\mathbf{N}$  is an  $N$  by  $N$  matrix sampled inside the RP, with a probability of occurrence  $P_k = n_k/N_{\text{tot}}$ , where  $n_k$  is the number of occurrences of the microstate and  $N_{\text{tot}}$  is the total number of possible configurations of 0 and 1 of the microstate (see Ikuyajolu et al., 2021, and Prado et al., 2020, for more details). The IE

is then defined as

$$\text{IE}(N_{\text{tot}}) = -\sum_{k=1}^{N_{\text{tot}}} P_k \ln P_k, \quad (2)$$

where  $k$  refers to the  $k$ th microstate. When IE is normalized by the maximum entropy (corresponding to when all microstates show the same probability), then  $\text{IE} = 0$  corresponds to perfect predictability and  $\text{IE} = 1$  represents chaos. Furthermore, the explicit dependence of the entropy quantifier on  $\epsilon$  is removed using the maximum entropy formulation. Prado et al. (2020) have shown that a value for which IE is maximum exists, does not vary much with varying  $\epsilon$ , and is strongly correlated with the Lyapunov coefficient of the system. We refer the reader to Ikuyajolu et al. (2021) for details of the heuristic used to estimate the maximum entropy. In essence, Prado et al. (2020) suggest a technique to eliminate the dependence of the entropy computation on the selection of a distance threshold  $\epsilon$  by finding a clearly defined maximum ( $S_{\text{max}}$ ) in the relationship between  $\epsilon$  and the entropy (see Fig. 4 in Prado et al., 2020). This maximum is robust and relatively stable within a range of  $\epsilon$  values. Furthermore, there is a strong correlation between the maximum entropy and the Lyapunov exponent. In our work, the code used to compute the entropy (see the “Code and data availability” section) uses the heuristic explained in Ikuyajolu et al. (2021) for the calculation of  $S_{\text{max}}$  through an iterative procedure that calculates the recurrence entropy for varying  $\epsilon$  until a maximum is found and retained. This algorithm requires three input parameters: the microstate dimension (set at 4 in this work, but we explored other values as shown in the Results section), the number of random samples to compute the microstate distribution in the RP (here 10 000), and a random sub-sample used to determine the  $\epsilon$  value for which the entropy is maximum (here 1000). We compute the entropy field of the deseasonalized and detrended IPV\* (full signal) using monthly data over all historical and future periods. At each point, the entropy of the IPV\* field is associated with recurring microstates in its time series (which defines the system and thereby impacts its predictability). The higher the predictability of a time series is, the more recurrent its temporal dynamics are, i.e., the easier it will be to predict its future evolution.

$\delta$ -MAPS (Fountalis et al., 2018) is used to identify climate modes of variability. It is an unsupervised network analysis method that identifies spatially contiguous and possibly overlapping regions referred to as domains and the lagged functional relationships between them. This dimensionality-reduction method is simpler and easier to interpret than empirical orthogonal functions (EOFs), which suffer from orthogonality constraints (Dommengot and Latif, 2002). Its benefits relative to conventional EOF-based approaches include interpretability and prevention of overfitting when extracting climate patterns from high-dimensional datasets (Falasca et al., 2019). In short,  $\delta$ -MAPS domains are spatially contiguous regions that share a highly correlated temporal activity between grid cells. In this work, we apply  $\delta$ -

MAPS to the sea surface temperature (SST) anomaly field (see the “Code and data availability” section) to identify major modes of climate variability in the North Pacific in a reanalysis and in the ESMs. Given any spatiotemporal field, its local homogeneity is hypothesized to be highest at “epi-centers” or “cores”. For each grid point, a local homogeneity is defined as the average pairwise cross-correlation between that grid cell and a set of  $K$  nearest neighbors (see Fountalis et al., 2018, for details). Cores are then determined as neighbors of points where the local homogeneity is a local maximum and above a threshold  $\delta$ . Each core is iteratively expanded and merged using a greedy algorithm to iteratively find domains as large as possible that are (i) spatially contiguous, (ii) include at least one core, and (iii) have homogeneity higher than  $\delta$ . Using a significance test,  $\delta$  is computed for the unlagged cross-correlations. Given any random pair of grid points, the significance of the Pearson correlation of their time series is assessed through Bartlett’s formula (Box et al., 2011), with the null hypothesis of no coupling. The significance of each correlation is tested for a user-specified significance level  $\alpha$ , and  $\delta$  is computed as the average of the significant correlations. Here, we applied  $\delta$ -MAPS with  $K = 8$  and  $\alpha = 0.01$ .

Lastly, we adopt the approach introduced by Diffenbaugh and Giorgi (2012) (which builds on Williams et al., 2007; Diffenbaugh et al., 2008; and references therein) to identify hotspots of change. The SED is a non-parametric method, meaning that it does not assume a specific probability distribution for the data. This flexibility makes it applicable to a wide range of datasets, regardless of their underlying distribution. The reader is referred to Turco et al. (2015) for its application to global atmospheric data. Here we apply the procedure described in Turco et al. (2015) to  $O_2$  and IPV\* as follows: hotspots are quantified through a standard Euclidean distance (SED) index that aggregates the changes in means, variability, and extremes of the given spatiotemporal field according to

$$SED = \sqrt{\sum_{i=1}^{N_{\Delta}} \sum_{j=1}^4 \left( \frac{\Delta_{ij}}{p_{95}(|\Delta_{ij}|)} \right)^2}. \quad (3)$$

We compute two SED indices in each grid point, separately for  $O_2$  and IPV\*.  $N_{\Delta}$  is the total number of indicators per variable and  $i$  is the index identifying each indicator;  $j$  spans the seasons, so  $\Delta_{ij}$  is the  $i$ th indicator in the  $j$ th season; and  $p_{95}$  is the 95th percentile. The indicators and SEDs are computed point by point; i.e., each grid point has one value. Therefore, the percentile is computed spatially over all the grid points. Here we consider December–January–February (the boreal winter, March–April–May spring, and so on. We consider three indicators for each variable, evaluating changes in means, variability, and extremes between two periods of equal length. *Period 1* covers 1950 to 1981 (1960 to 1986 for the reanalysis and the E3SM-2G ocean hindcast). *Period 2* covers 1983 to 2014 (1988 to 2014 for the reanalysis

and the hindcast) over the historical time frame and 2036 to 2067 and 2069 to 2100 for the projected future. In Eq. (3), indicators of both periods are normalized to the 95th percentile calculated over period 1 to fairly compare changes in the intensity of hotspots over time. We chose not to compare the period from 2069 to 2100 with the period from 1950 to 1981 but rather to compare it to 2036 to 2067 instead because we wish to track changes in each period compared to the preceding time slot to quantify how rapidly they occur in the future projections compared to the historical time frame. For each variable, we compute three indicators at each grid point and for each season using the Climate Data Operators (CDO; Schulzweida, 2022) as follows.

Changes in means are estimated in each season separately by  $\Delta_{\text{means}} = y_{\text{seasm}_2} - y_{\text{seasm}_1}$ , where  $y_{\text{seasm}_1}$  and  $y_{\text{seasm}_2}$  are the multi-year seasonal means in periods 1 and 2, respectively. Therefore, taking for example the  $O_2$  historical simulations over the period from 1950 to 2014 (although similar expressions also hold for IPV\* and the other periods),  $\Delta_{\text{means DJF}} = \langle O_{2\text{DJF}} \rangle_{1983-2014} - \langle O_{2\text{DJF}} \rangle_{1950-1981}$ ,  $\Delta_{\text{means MAM}} = \langle O_{2\text{MAM}} \rangle_{1983-2014} - \langle O_{2\text{MAM}} \rangle_{1950-1981}$ ,  $\Delta_{\text{means JJA}} = \langle O_{2\text{JJA}} \rangle_{1983-2014} - \langle O_{2\text{JJA}} \rangle_{1950-1981}$ , and  $\Delta_{\text{means SON}} = \langle O_{2\text{SON}} \rangle_{1983-2014} - \langle O_{2\text{SON}} \rangle_{1950-1981}$ , where  $\langle \dots \rangle$  is a time mean (seasonal climatology).

Changes in multi-year seasonal variability  $\Delta_{\text{variability}}$  are evaluated by (i) detrending each variable point by point in the two periods separately; (ii) computing the multi-year seasonal standard deviation of these detrended fields,  $y_{\text{seas}\sigma}$ , for each period for each season; and (iii) computing as the percent changes such that  $\Delta_{\text{variability}} = 100 \cdot \left( \frac{y_{\text{seas}\sigma_2} - y_{\text{seas}\sigma_1}}{y_{\text{seas}\sigma_1}} \right)$ . Therefore, with the example of  $O_2$  historical simulations over the period from 1950 to 2014,  $\Delta_{\text{variability DJF}} = 100(\text{std}(O_{2\text{DJF}})_{1983-2014} - \text{std}(O_{2\text{DJF}})_{1950-1981}) / \text{std}(O_{2\text{DJF}})_{1950-1981}$ , where  $\text{std}(\dots)$  is the multi-year seasonal (winter) standard deviation over the specified period (equivalent formulations also hold for the other seasons).

Finally, changes in extremes (in our case overshoots of IPV\* and undershoots of  $O_2$ ) are computed through the following steps: (i) for each season, we compute at each grid point the multi-year  $O_2$  minimum or IPV\* maximum over period 1 using monthly data (e.g., the  $O_2$  minimum given all December, January, and February values for the boreal winter), and we build a threshold map for each season; (ii) we count how many times  $O_2 < \text{threshold}_{O_2}$  (or  $\text{IPV}^* > \text{threshold}_{\text{IPV}^*}$ ) is verified in each corresponding season of period 2, again using monthly data; and (iii) the percentage of occurrences computed in point (ii) is finally taken as an indicator of percent changes in extremes and estimated by  $\Delta_{\text{extremes}} = 100 \times \left( \frac{N_{\text{occ}}}{N_{\text{T}}} \right)$ , where  $N_{\text{occ}}$  is the number of extreme occurrences (in each season) and  $N_{\text{T}}$  is the total number of months in the corresponding seasons (96 for the models and 81 for reanalysis and hindcast).



Building on previous works (Falasca et al., 2019; Falasca and Bracco, 2022), we expect the statistics of a given model to remain relatively stable across ensemble members; i.e., we do not expect the member choice to significantly influence the calculation of extremes and hotspots or their relationships in particular. We verified that this is indeed the case in one of the models by testing four additional randomly chosen ensemble members of CanESM5 (see the “Code and data availability” section). A major advantage of this hotspot definition is that it accounts for changes in the mean, variability, and extremes at the same time. In other words, it accounts for the intrinsic characteristics of the simulated climate fields, which can be characterized by considering all three aspects together. In particular, the definition of extremes aims at including information on months exceeding corresponding seasonal baseline extremes, without choosing a threshold on the current distribution a priori, which is especially relevant for comparing changes with respect to a reference baseline. The three indicators, grouped into four seasons for each variable, are then used to compute the SED indices.

Finally, IPV\* ( $\text{m}^{-1} \text{s}^{-1}$ ) is used as a proxy for stratification and is defined as the isopycnic potential vorticity (Talley et al., 2011) with the absolute value of the Coriolis parameter in its formula:

$$\text{IPV}^* = \frac{|f|}{g} N^2. \quad (4)$$

Here,  $N^2$  is the Brunt–Väisälä frequency ( $-\frac{g}{\rho} \frac{\partial \rho}{\partial z}$ ), which measures the fluid stability to vertical displacements;  $g$  is the gravitational acceleration;  $f$  is the Coriolis parameter; and  $\rho$  is the density, calculated in this work using salinity and temperature fields and the TEOS-10 equation of state for seawater (<http://www.teos-10.org/>, last access: 17 April 2024). IPV is a conservative tracer in frictionless and adiabatic circulation. IPV\* is calculated over the three-dimensional ocean volume using Eq. (4) considering the 0–200 m vertical weighted average. This procedure allows us to compare datasets with different vertical discretization.

### 3 Data

We consider four ESMs from the CMIP6 historical catalogue (with prescribed  $\text{CO}_2$  concentrations), a hindcast, and reanalysis data, as summarized in Table 1. Whenever multiple ensemble members were available, we selected the first (r1i1p1f1). We randomly selected four additional ensemble members for CanESM5 (r5i1p1f1, r10i1p1f1, r15i1p1f1, and r20i1p1f1) to further verify the robustness of the hotspot calculation to the member choice. All ESMs are forced with prescribed  $\text{CO}_2$  concentrations from 1850 to 2014, and we analyze the monthly outputs from 1950 to 2014. We further discuss future SSP5-8.5 scenarios and focus on the 2036 to 2100 period, indicated as *future*.

The hindcast is a new ocean–ice biogeochemistry simulation (referred to as the G-Case) E3SMv2.0-BGC (hereafter E3SM-2G; Takano et al., 2023) based on the Model for Prediction Across Scales – Ocean (MPAS-O), an ocean component of the Energy Exascale Earth System Model (E3SM) version 2 (Golaz et al., 2022). Details on ocean physics updates can be found in Golaz et al. (2022). One of the major updates is the introduction of Redi isopycnal mixing (Redi, 1982). Along with ocean physics updates, this version also incorporated a uniform background vertical diffusion specifically developed for simulations of the ocean biogeochemistry to enhance ocean carbon uptake and thermocline ventilation of dissolved inorganic carbon (DIC). Incorporating this mixing parameterization results in improved representation of climatological  $\text{O}_2$  distributions in the v2.0 version compared to its predecessor (Burrows et al., 2020). The Marine Biogeochemistry Library (MARBL; Long et al., 2021) is used to simulate ecosystem dynamics and the cycling of biogeochemical elements. After the spin-up period, the model is forced by a meteorological reanalysis dataset, JRA55-do version 1.4 (Tsujino et al., 2020), from 1958 onward. As an ocean reanalysis, we use the ORAS4 product (Balmaseda et al., 2012; Mogensen et al., 2012) available from 1959 onward, which includes a direct surface flux implementation from ERA-40 and ERA-Interim and multi-scale bias correction. When analyzing the E3SM-2G hindcast and the ORAS4 reanalysis, we focus on the 1960 to 2014 interval to avoid the spurious presence of an anticyclonic tropical cyclone in the northeastern Pacific in 1959 in JRA55-do v1.4.

All the data, models, and reanalysis are remapped at  $1^\circ$  by  $1^\circ$  horizontal resolution and to a common vertical grid with a linear interpolator.

We begin our analysis with a brief evaluation of the ESM biases in the two main fields of interest, IPV\* and  $\text{O}_2$ . For IPV\*, the ocean reanalysis dataset is used for validating the model outputs for the maximum possible time overlap in the historical configuration (1959 to 2014). For  $\text{O}_2$ , we can only contrast the annual mean  $\text{O}_2$  climatology data between the World Ocean Atlas (Garcia et al., 2019) and the ESMs (Fig. 1). We additionally compared the ORAS4 IPV\* climatology data over the period from 1988 to 2014 (i.e., period 2 for this reanalysis) with the corresponding climatology data computed using SODA3.4.2, which uses a different ocean component to ORAS4. The differences across reanalyses that use different models but assimilate the same observations are much smaller (about 1 order of magnitude) than the signal (Fig. S1 in the Supplement) and smaller than any model bias.

The E3SM-2G hindcast is forced by observed atmospheric fields and displays the smallest bias and, for  $\text{O}_2$ , also the smallest root mean square error (RMSE), which is shown atop the panels in Fig. 1. Overall, the IPV\* and  $\text{O}_2$  biases have broadly anticorrelated patterns, with the models being generally less stratified and more oxygen rich than observed in the extratropical North Pacific and often too stratified and with a larger  $\text{O}_2$  deficit compared to observations south of the

**Table 1.** The CMIP6 Earth system models, global ocean hindcast, and reanalysis used in this work. Under each model name, a short form used in the following figures is indicated in parentheses.

Modeling group or center	Model name	Atmospheric component and resolution	Oceanic component and resolution	Reference
National Oceanic and Atmospheric Administration, Geophysical Fluid Dynamics Laboratory	GFDL-ESM4 (GFDL)	AM4.0, $\sim 1^\circ$ , 49 levels	OM4 MOM6, $0.5^\circ$ by $0.5^\circ$ , 75 vertical levels (hybrid pressure or isopycnal). Biogeochemical component: COBALTv2	Dunne et al. (2020), Stock et al. (2020)
Canadian Earth System Model version 5	CanESM5 (CanESM)	CanAM5, T63 ( $\sim 2.8^\circ$ ), 49 levels	CanNEMO, 45 vertical levels, NEMO3.4.1, ORCA1 tripolar grid, $1^\circ$ with refinement to $1/3^\circ$ within $20^\circ$ of the Equator. Biogeochemical component: CMOG	Swart et al. (2019), Christian et al. (2022)
NorESM Climate Modeling Consortium	NorESM2-LM (NorESM)	CAM-OSLO, $2^\circ$ resolution, 32 levels	MICOM, $1^\circ$ , 70 vertical levels. Biogeochemical component: iHAMOCC	Seland et al. (2020), Tjiputra et al. (2020)
Institut Pierre-Simon Laplace	IPSL-CM6A-LR (IPSL)	LMDZ, NPv6, N96; $1.25^\circ$ Lat $\times$ $2.5^\circ$ long, 79 levels	NEMO-OPA (eORCA1.3), tripolar primary $1^\circ$ , 75 vertical levels. Biogeochemical component: PISCESv2	Boucher et al. (2020)
Department of Energy, Energy Exascale Earth System Model	E3SMv2.0-BGC (E3SM)	JRA55-do reanalysis, 55 km, 3 h resolution	MPAS-O, 30 to 60 km resolution. Biogeochemical component: E3SMv2.0-BGC, MARBL	Golaz et al. (2022), Takano et al. (2023), Long et al. (2021)
ECMWF Ocean Reanalysis System	ORAS4	–	Global, $1^\circ$ , 42 levels	Balmaseda et al. (2012), Mogensen et al. (2012)

Equator. However, maximum and minimum biases in the two fields seldom coincide. Regionally, E3SM-2G is generally less stratified than observed, with a relatively low  $O_2$  bias and an overestimation of approximately  $10 \mu\text{mol kg}^{-1}$  in the subtropical thermocline of the North Pacific basin. The hindcast performs especially well in the tropical thermocline. Among the CMIP6 models, CanESM5 shows a slightly higher IPV\* underestimation in the subpolar gyre and an  $O_2$  overestimation in the subtropics compared to the other ESMs, while NorESM2-LM emerges as the most stratified south of the Equator. For  $O_2$ , larger biases (positive or negative) are generally found in the tropical thermocline and the tropical and subtropical boundaries. The sign and magnitude of the biases are model dependent. Interestingly, models generally overestimate  $O_2$  at subpolar latitudes.

## 4 Results

### 4.1 Predictability potential (HYP 1)

We begin our analysis by considering the predictability potential of IPV\* as quantified through the information entropy

(IE; see “Materials and methods”). The goal is to verify if and where IPV\* has an elevated predictability owing to the presence of quasi-recurrent behaviors in its time series. We also aim to examine whether  $O_2$  is correlated with IPV\* in regions where the latter has a high predictability potential. As a reminder, IE values close to 1 indicate high complexity and unpredictability, and values close to 0 indicate perfect predictability (the signal is recurrent, e.g., constant or periodic). We preliminarily tested the sensitivity of the entropy field to the microstate dimension within a range that is meaningful according to previous literature (Ikuyajolu et al., 2021) using microstates of dimensions 2, 3, 4, and 5 for GFDL over the period from 1950 to 2014 (Fig. S2). We found that the IE pattern, i.e., areas more (or less) predictable relative to the surroundings, is substantially unchanged and that the geographical patterns are robust to changes in the microstate dimension, in agreement with Ikuyajolu et al. (2021). Both microstate dimension 4 and microstate dimension 5 show reasonable entropy values, and we chose to use a microstate dimension of 4 to conduct our analysis because it spans the widest range of possible values.

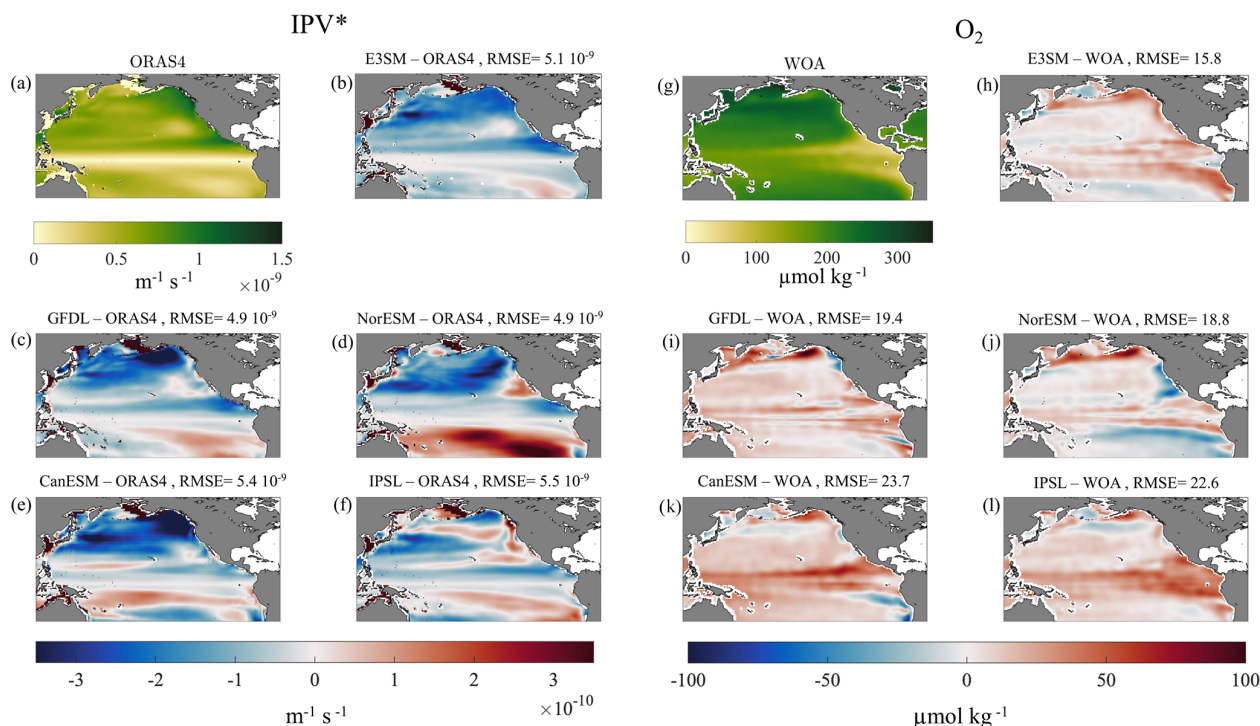


**Figure 1.** (Left) IPV\* annual climatology means (1959 to 2014) weighted-averaged over 0–200 m depth in the North Pacific basin. (a) ORAS4. (b–f) Model bias (model – ORAS4) differences. (Right) O<sub>2</sub> annual climatology means (1950 to 2014) weighted-averaged over 0–200 m depth. (g) World Ocean Atlas (WOA) climatology means. (h–l) Model biases (model – WOA) difference. The root mean square error (RMSE) values of the modeled IPV\* ( $\text{m}^{-1} \text{s}^{-1}$ ) and O<sub>2</sub> ( $\mu\text{mol kg}^{-1}$ ) are shown for each panel.

#### 4.1.1 O<sub>2</sub>–IPV\* relationship across ESMs and its future evolution

IE maps for IPV\* are shown in Fig. 2 for both historical and future time frames, with superposed contours of the areas where the (lagged) anticorrelation between IPV\* and O<sub>2</sub> is at least  $-0.5$  (see Figs. S3–S4 for the anticorrelation and lag maps). Higher predictability in the historical period is found in the tropical Pacific areas close to the geographical location of ENSO (i.e., the area most impacted by the domain identified as ENSO-related by  $\delta$ -MAPS, which maps well the region identified by an EOF analysis over the SST field for having the greatest variance explained by the first principal component, pc1). The predictability potential is generally highest along two stripes enclosing the ENSO pattern north and south of the Equator and excluding the upwelling cold tongue. The distribution of IE follows broadly that found in a much longer simulation of the IPSL model covering the past 6000 years and analyzed by Falasca et al. (2020), and it appears to be robust across models. The western boundary current region and the Kuroshio–Oyashio Extension have low predictability across all datasets considered. In NorESM2-LM and CanESM5, and to a lesser degree in ORAS4 and IPSL-CM6A-LR, the higher predictability of the ENSO area extends to the northeastern portion of the basin. In general, in both the hindcast and the models,

strong anticorrelations between IPV\* and O<sub>2</sub> (correlation coefficient (c.c.)  $\leq -0.5$ ) coincide with regions of low IE and are linked to ENSO affecting stratification and O<sub>2</sub> concurrently in the tropics and south of the upwelling area. Very limited IPV\* predictability is found in the central and western North Pacific, where the variability is dominated by the PDO signal. The PDO does not emerge as easily predictable in the interval considered, in agreement with, e.g., Gordon et al. (2021) and Falasca et al. (2020), who analyzed the predictability of sea surface temperatures in the IPSL model across the whole second half of the Holocene. In those areas, anticorrelations between O<sub>2</sub> and IPV\* are relatively weak (generally  $> -0.4$  except for NorESM). The entropy and the regions where the evolution of IPV\* and O<sub>2</sub> are strongly anticorrelated do not change significantly in the future projections of the four models. We further explored whether oxygen solubility (O<sub>2sol</sub>), which is modulated by ocean warming and cooling, and the apparent oxygen utilization (AOU), which is controlled mostly by the biogeochemical processes affecting oxygen demand, may be independently linked to IPV\* predictability. The areas in which IPV\* and AOU time series are positively correlated, with correlation coefficients  $\geq 0.5$ , are very similar to the ones obtained by analyzing the O<sub>2</sub>–IPV\* relationship. For O<sub>2sol</sub>, which approximates preformed O<sub>2</sub> at the depths considered well, the anticorrelation areas (i.e., where c.c.  $\leq -0.5$ ) are quite extensive, especially

in the hindcast, but mostly superimposed onto high-entropy and low-predictability IPV\* areas (Fig. S5).

In Fig. S6 we show the IE maps for O<sub>2</sub>. Predictability is generally higher outside the equatorial upwelling region and the Kuroshio–Oyashio Extension. In E3SM, the areas in which the predictability potential of IPV\* is high and the correlation with O<sub>2</sub> is  $\leq 0.5$  coincide and also have low IE in O<sub>2</sub>. This is verified to some extent in IPSL and NorESM but not in the other two models.

In the next section we isolate the PDO signal to explore whether the low predictability in the North Pacific (north of ENSO region) is related to the superposition of different timescales, i.e., whether there is low-frequency PDO modulation with high-frequency “noise” due to both atmospheric and oceanic variability. The PDO is indeed a lower-frequency mode compared to ENSO and has most loading at extratropical latitudes in which the atmospheric “noise” is greater.

#### 4.2 Trends and PDO impact on O<sub>2</sub> and IPV\* (HYP 2)

The limited predictability found in the North Pacific does not exclude the possibility of the PDO modulating both IPV\* and O<sub>2</sub> inventories simultaneously. As explored in previous work (e.g., Ito et al., 2019), the dominant mode of observed O<sub>2</sub> variability in the northern Pacific Ocean is indeed correlated with the PDO index, which explains about 25 % of the variance. Observations, however, offer only sparse coverage in both time and space. To further verify the PDO modulation, we computed the first EOF for the E3SM-2G hindcast 0–200 m O<sub>2</sub> and IPV\* anomalies for the period from 1960 to 2014 over the northern Pacific (20.5–69.5° N 115.5° E–60.5° W) and the corresponding time series for pc1. The first EOF explains 25 % of the oxygen variance and about 12 % of the IPV\* variance. The computed pc1 shows a significant and strong correlation (Pearson’s *R* coefficient) with the PDO time series computed using SST anomalies, with  $|R| = 0.83$  ( $p < 0.01$ ) for O<sub>2</sub> and  $|R| = 0.44$  ( $p < 0.01$ ) for IPV\* after applying 5-year moving means. The correlation with the PDO is higher than with the ENSO, which is at most  $|R| = 0.34$  ( $p < 0.01$ ) for O<sub>2</sub> after applying a 3-month moving mean, consistent with the analysis by Ito et al. (2019). We hereby quantify the (linear) impact of the PDO on the two fields of interest and then evaluate their residuals. If the PDO is the main predictor of IPV\* and O<sub>2</sub> distributions, its impact on the two fields should be strongly anticorrelated and larger than the residual. As mentioned above, the objective is to verify whether IPV\* could be used to extrapolate information about O<sub>2</sub> and its evolution in time, bypassing – at least to some degree – the need to run full biogeochemical models or measure O<sub>2</sub> directly.

#### 4.2.1 Estimation of climate indices and their relationship with IPV\* and O<sub>2</sub>

We use  $\delta$ -MAPS (see “Materials and methods”) applied to the SST field to evaluate the main modes of Pacific climate variability, i.e., ENSO and PDO, and their time evolution in the models, in the ocean hindcast, and in the reanalysis. While the evolution of ENSO using  $\delta$ -MAPS is straightforwardly described by the time series of the cumulative anomalies in the ENSO-related domain (e.g., Falasca et al., 2019), for the PDO we must consider the difference between the SST cumulative anomalies of two domains. The domains are identified by the complex network algorithm, and we applied a 5-year running mean to produce the PDO time series shown in Fig. 3. The shape and size of the domains are indicated in Fig. 4. For ORAS4 and E3SM-2G over the period from 1960 to 2014, we computed the 0-lag Pearson’s correlation coefficients between these time series and the commonly defined indices of PDO (following Mantua et al., 1997) and Niño 3.4 (average SST anomalies over the box 5° N–5° S, 170–120° W) retrieved from NOAA (<https://psl.noaa.gov/data/climateindices/list/>, last access: 17 April 2024). After applying a 3-month moving average to the ENSO time series (signals and indices) and a 5-year moving average to the PDO time series (signals and indices), the correlation coefficients are 0.88 for PDO and 0.93 for ENSO in ORAS4 and 0.89 for PDO and 0.91 for ENSO in E3SM-2G.

Among the models (Fig. 3), GFDL slightly underestimates the PDO strength during the historical period, while the opposite is true of CanESM and NorESM. In the latter, the frequency of the signal is also higher than observed. By the end of the 21st century, the strength of the PDO remains unaltered in GFDL and IPSL, while it decreases in NorESM2 and especially in CanESM following a decrease in the size of the eastern domain. A decrease in amplitude and an increase in frequency of the PDO were also found in several models in the CMIP5 ensemble (Li et al., 2020).

Given the PDO(*t*) indices, the residual component of the fields of interest that is not linearly forced by the PDO can be separated as a function of time (see, e.g., Kucharski et al., 2008) so that for O<sub>2</sub> (but the same procedure was applied to IPV\*)

$$O_{2\text{res}}(x, y, t) = O_2(x, y, t) - O_{2\text{PDO}}(x, y, t), \quad (5)$$

where

$$O_{2\text{PDO}}(x, y, t) = b_{O_2}(x, y) \cdot \text{PDO}(t). \quad (6)$$

The parameter  $b_{O_2}(x, y)$  is constant over time and determined by least-squares fitting through a linear regression for each dataset separately. Figure 4 shows  $b_{\text{IPV}^*}$  and  $b_{O_2}$  for all datasets with the boundaries of the domains corresponding to the ENSO mode and those contributing to the PDO in the historical period superposed. In most cases there is an overall anticorrelation between the maps of the two fields, but there

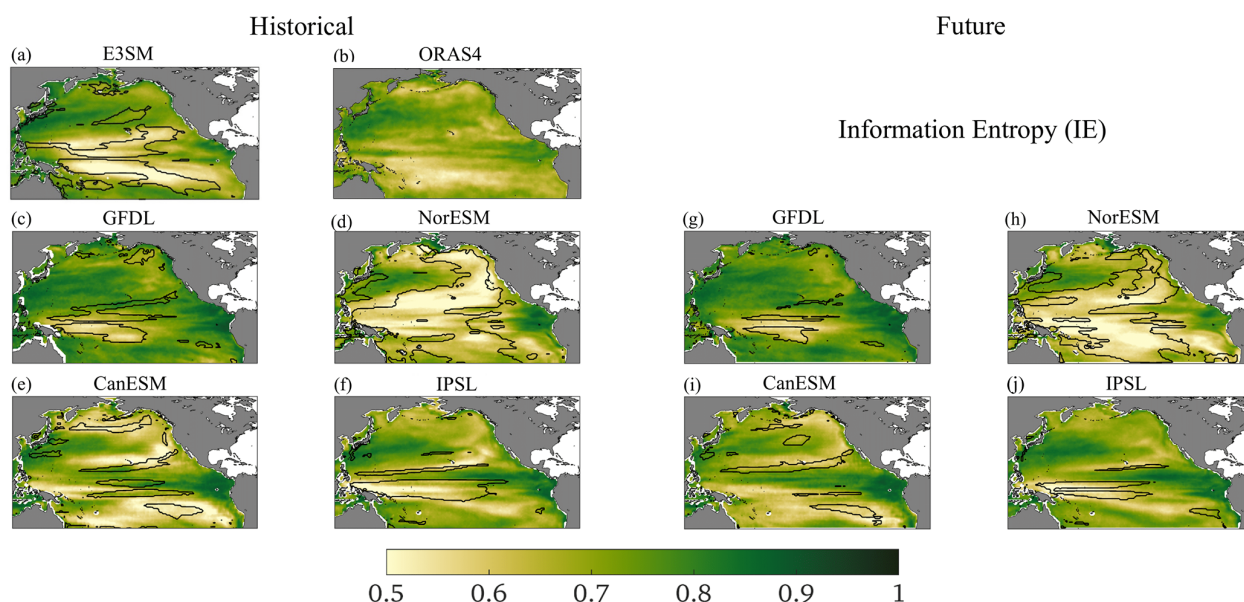


**Figure 2.** IPV\* information entropy in the historical interval (left) and in the future (right) for the ESMs and in the historical period from 1960 to 2014 for the hindcast and ORAS4, with superposed contours of the areas where in which the IPV\* and O<sub>2</sub> time series are anticorrelated, including correlation coefficients  $\leq -0.5$ .

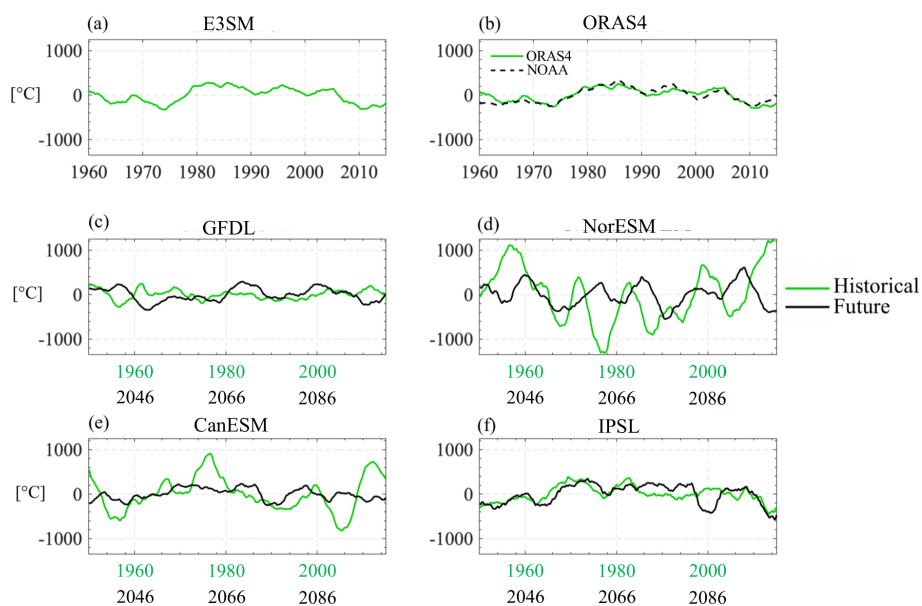


**Figure 3.** PDO indices (SST cumulative anomalies) calculated using  $\delta$ -MAPS (see text) in the historical and future time frames. The dashed line in panel (b) is the PDO index time series from NOAA (available at <https://psl.noaa.gov/data/climateindices/list/>, last access: 17 April 2024) multiplied by the standard deviation of the ORAS4 time series in panel (b) after applying a 5-year moving mean.

are also several important differences. First, the regions in which  $b_{O_2}$  is strongest (both positive and negative values) do not correspond to minima and maxima in  $b_{IPV^*}$ . Second, the equatorial upwelling tends to have a strong positive signal in  $b_{O_2}$  and only a weak one, albeit of the same sign, in  $b_{IPV^*}$ . Third, the impacts of PDO on the fields vary substantially among models, as quantified by the correlations among the

respective fields indicated atop the  $b_{O_2}$  plots, with GFDL being the closest to the hindcast and, for the IPV\* case, also to the reanalysis. In NorESM2 the anticorrelation between the regression fields is too strong and the PDO has both a shape and a loading different to those observed in the Pacific interior. CanESM and IPSL display positive spatial correla-

tions, with important biases with respect to the hindcast at the Equator and along the eastern boundary.

We performed a comparable linear regression analysis using the ENSO index instead of the PDO and, as expected, obtained similar shapes of the  $b$  coefficients but much lower absolute values (Fig. S8). This further confirms that in the North Pacific, the PDO is the dominant mode of climate variability.

Moving on to the projections, the maps of the regression coefficients do not change considerably in three of the models considered (Fig. 5). In CanESM, on the other hand,  $b_{IPV^*}$  changes sign over most of the domain. The residual trends, when compared to the regression coefficients, are stronger and dominate the evolution of both fields, especially in the subtropical and subpolar gyres of the North Pacific (Fig. S9), thereby superseding the PDO signal.

Overall, during the historical period, the residuals have an amplitude comparable to the PDO-forced signal (see Fig. S7), and the linear trends have similar patterns to but lower amplitude than the whole-field trends (see further discussion of trend shape when presenting  $\Delta_{\text{means}}$ ). In the future, on the other hand, linear trends of residuals and whole fields have similar patterns and intensities.

### 4.3 Hotspots of change (HYP 3)

As a last step, we evaluate changes in means, variability, and extremes for both variables (considering whole signals, i.e., not just the residuals) using the indicators introduced in “Materials and methods”. For the historical time frame, we divide the interval from 1950 to 2014 into two periods of equal length covering 1950 to 1981 and 1983 to 2014 (1960 to 1986 and 1988 to 2014 for E3SM-2G and ORAS4). We evaluated the indicators in each season separately or averaged together and found that differences across seasons were small, as measured by the standard deviation of the indicators (Figs. S10–S12). In the following we discuss only the indicators averaged across the four seasons without loss of information.

The representations of  $\Delta_{\text{means}}$  in Fig. 6 show the changes in the mean fields, which have very similar patterns to the linear trend in both  $IPV^*$  and  $O_2$  (see Fig. S7). By 2015, stratification has increased nearly everywhere in the ESMs, except for the equatorial upwelling region and the Kuroshio–Oyashio Extension. In ORAS4 there is also a prominent band in which stratification decreases between 10 and 20° N from the coast of the American continent to 150° W in the second period and in the overall trend.  $O_2$  decreases in most of the North Pacific, especially in the subpolar gyre around the Kamchatka Peninsula, and increases in the upwelling areas along the coasts of Peru and Central America as well as in the California Current System. Regions of increasing  $O_2$  are also found corresponding to the North Equatorial Current in the E3SM-2G hindcast and in the GFDL and CanESM models, in the equatorial upwelling band in NorESM2, and in por-

tions of the subpolar gyre around Alaska in E3SM-2G and IPSL.

Indicators of change in (seasonal) variability ( $\Delta_{\text{variability}}$ ; Fig. 7) show strong differences across models in terms of patterns and, at least for  $O_2$ , intensity. Whenever corresponding maps of  $O_2$  and stratification have the same sign and comparable amplitude at corresponding locations, they indicate that increments or decreases in  $IPV^*$  variability at seasonal scales are associated with corresponding increments in 0–200 m  $O_2$  variability. In the hindcast, changes are greater for residual  $O_2$  than for stratification. This is verified in three of the models in the northeastern extratropics. Among the models, GFDL and NorESM2 show patchy changes, both positive and negative, across the domain, with the smallest amplitudes among the datasets considered. CanESM undergoes predominately positive changes north of the Equator in  $IPV^*$  and negative changes to the south of it, while the variability in the  $O_2$  field also decreases in the central portion of the subtropical gyre. In IPSL the variability increases nearly everywhere in both fields but especially at the Equator and to the south of it in  $IPV^*$  and more uniformly at all latitudes in  $O_2$ .

Changes in extremes ( $\Delta_{\text{extremes}}$ ) for the  $O_2$  field are stronger than for stratification (Fig. 8). Episodes of strong  $O_2$  decrease and stratification increase are more frequent in period 2. For  $O_2$  the regions to the north and south of the equatorial upwelling band emerge as most impacted in the E3SM-2G hindcast and GFDL, while the subtropical gyre displays an increase in extreme events nearly everywhere in CanESM and IPSL, at its boundary in E3SM-2G, and in its eastern portion in GFDL and NorESM. The subpolar gyre is affected especially in CanESM and IPSL. Changes in  $IPV^*$  extremes have less clear latitudinal differences and do not display a robust intensification at extratropical latitudes across the models. In ORAS4, maxima are found near the California Current System and in the warm-pool area.

Table 2 summarizes the correlation coefficients between the maps of the three indicators for the two fields considered. Coefficients are negative for all models but small for  $\Delta_{\text{means}}$ ; slightly larger in amplitude and positive for the variability indicator ( $\Delta_{\text{variability}}$ ); and very small for  $\Delta_{\text{extremes}}$  in the hindcast, CanESM, and IPSL analyses, while they are larger in amplitude and positive for GFDL, with a strong contribution from the equatorial region, especially in NorESM, where positive values are also found north of 20° N.

The resulting hotspot indices (SED), computed separately for the  $IPV^*$  and the  $O_2$  indicators (see “Materials and methods”), are reported in Fig. 9. Except for IPSL, the hotspots are found outside the equatorial band. Those for  $O_2$  are generally stronger along the eastern part of the subtropical gyres, in the eastern part of the PDO region, and along the California upwelling system, and the  $IPV^*$  hotspots are more commonly found over the western parts of the basin and along the southern boundary of the subtropical gyre. This result suggests a longitudinal decoupling between hotspots in  $O_2$  and



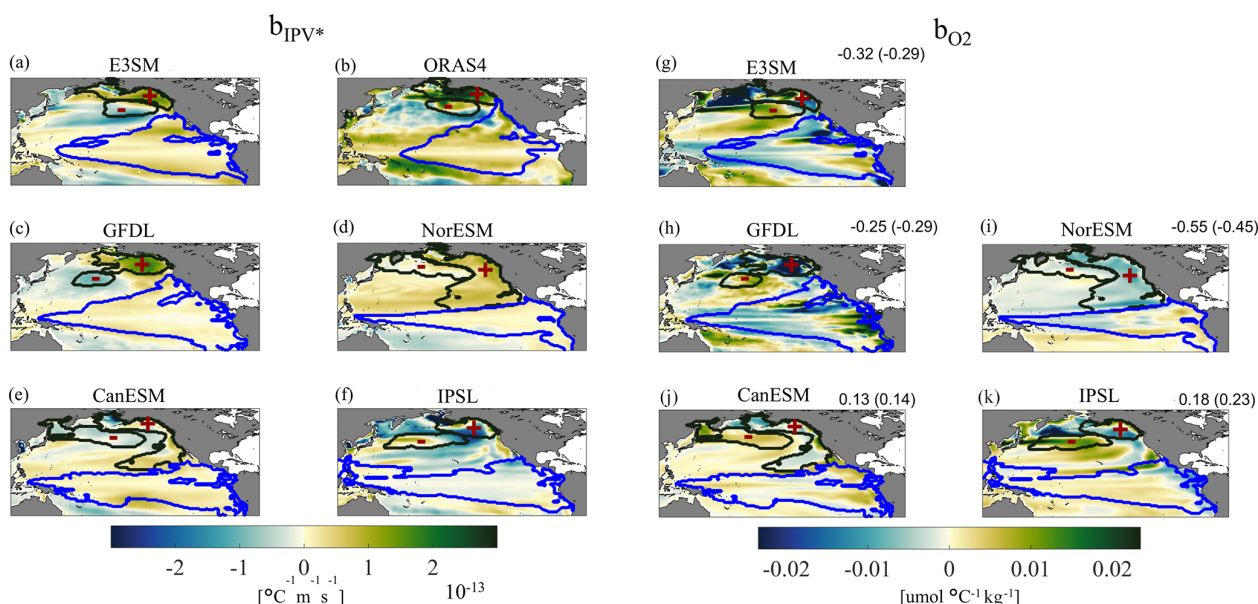


**Figure 4.**  $b_{IPV^*}$  (left) and  $b_{O_2}$  (right) regression coefficient maps with superposed contours of the ENSO (blue line) and of the PDO+ and PDO– domains.  $b_{IPV^*}$  represents the change in  $IPV^*$  per unit change in SST, and  $b_{O_2}$  represents the change in  $O_2$  per unit change in SST. The correlation coefficients (c.c.'s) among the corresponding maps for the same model or hindcast are also indicated. Color limits are fixed as  $\pm 3$  standard deviations of the ensemble for each variable over the whole area ( $\pm 2.99 \times 10^{-13}$  for  $IPV^*$  and  $\pm 0.023$  for  $O_2$ ). Values in parentheses are c.c.'s computed north of  $20^\circ$  N. All c.c.'s passed a shuffling significance test at the 5 % level (see Supplement).

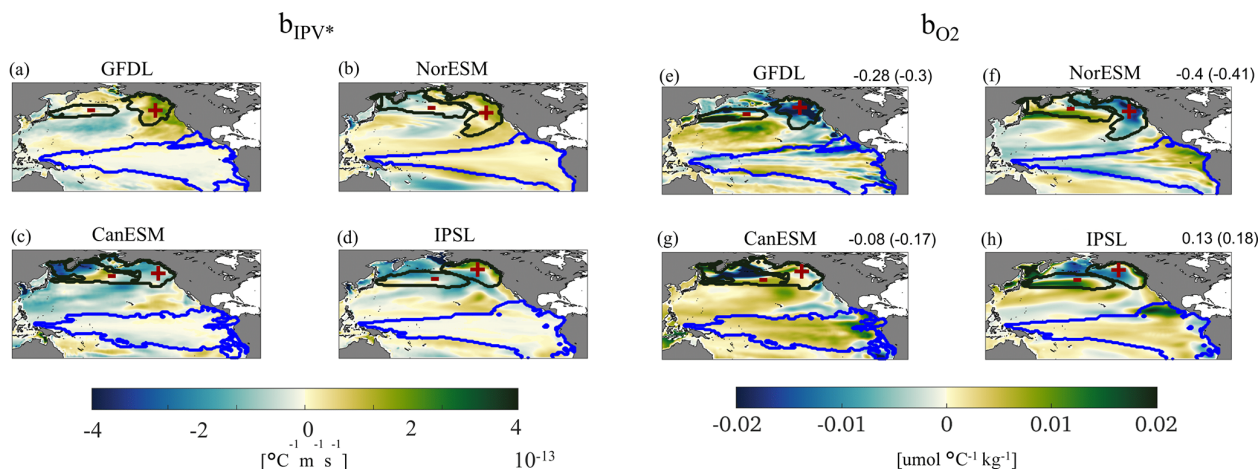


**Figure 5.** As in Fig. 4 but for the future projections. Color limits are fixed as  $\pm 3$  standard deviations of the ensemble for each variable over the whole area ( $\pm 4.1 \times 10^{-13}$  for  $IPV^*$  and  $\pm 0.02$  for  $O_2$ ). Values in parentheses are correlation coefficients (c.c.'s) computed north of  $20^\circ$  N. All c.c.'s passed a significance test at the 5 % level (see Supplement).

stratification in at least three of the models and in the hindcast, with NorESM being the exception due to the simulated superposition of the changes in extremes in the two fields. We also computed the SED for the residual fields, obtaining similar results (Fig. S13).

The maps of the indicators for the future projections follow in Figs. 10–12, again averaged over seasons, and the associated standard deviations are reported in Figs. S14–S16. In the projections, the seasonal differences are slightly greater

compared to the historical period for  $\Delta_{\text{means}}$  ( $IPV^*$ ) in the northern subpolar gyres, especially for CanESM, NorESM, and IPSL (Fig. 10), and along the subtropical and the northern subpolar gyres for  $\Delta_{\text{extremes}}$  ( $IPV^*$ ) (Fig. 12). Standard deviations for  $\Delta_{\text{extremes}}(O_2)$  are stronger along the extratropical gyres and weaker in the tropical upwelling region (Fig. S16). Areas of higher standard deviations in the projections are, however, associated with much stronger values of  $\Delta_{\text{means}}$  and  $\Delta_{\text{extremes}}$  compared to the historical period.



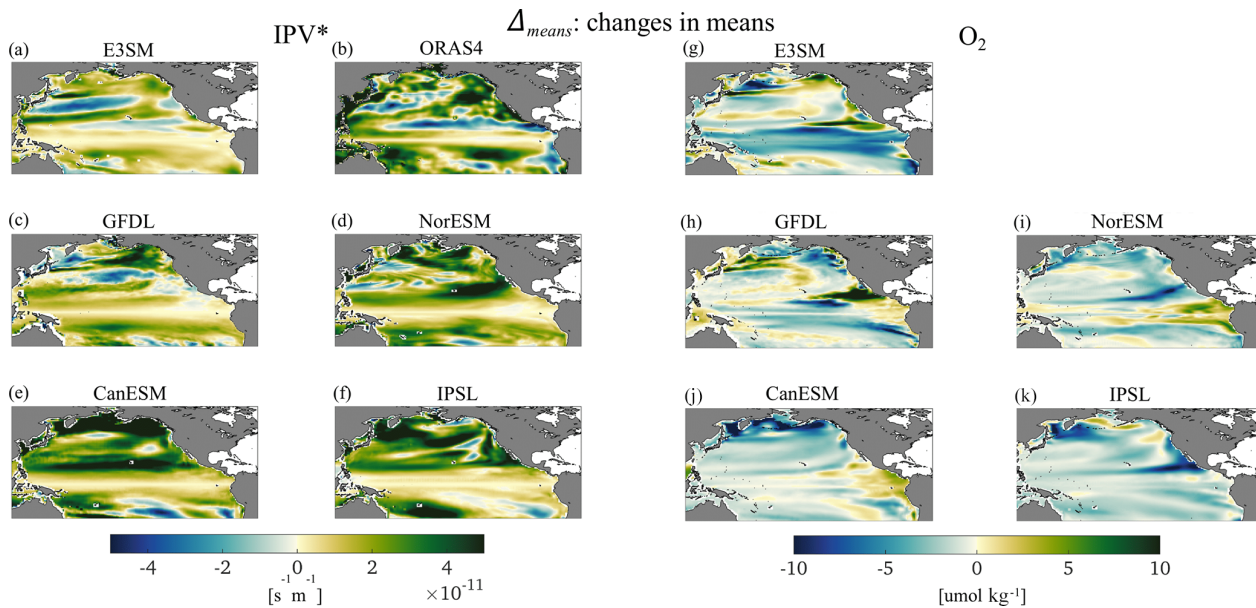


**Figure 6.** For the period from 1950 to 2014,  $\Delta_{\text{means}}$  for IPV\* (left) and O<sub>2</sub> (right). All indicator maps are obtained by averaging the respective seasonal maps.

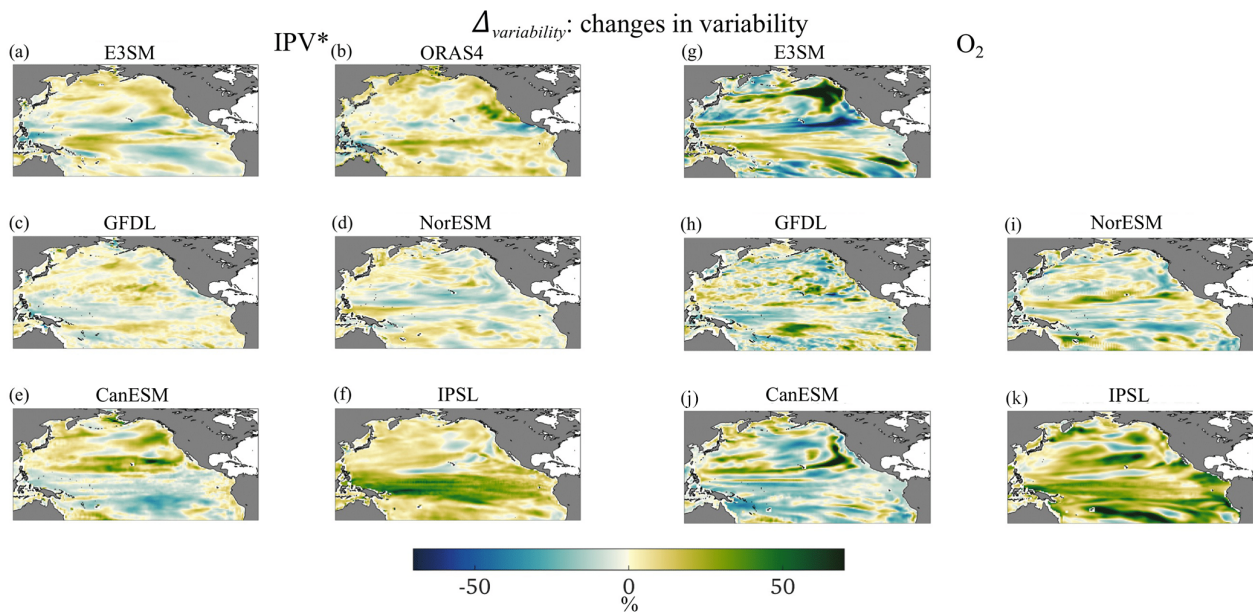


**Figure 7.** For the period from 1950 to 2014,  $\Delta_{\text{variability}}$  for IPV\* (left) and O<sub>2</sub> (right).

In the projections,  $\Delta_{\text{means}}$  strengthens significantly and is stronger than the actual trend shown in Fig. S9, indicating an acceleration of the changes in the last portion of the 21st century. This is especially relevant for IPV\* north of the Equator. Stratification increases everywhere except for regions in the Southern Hemisphere with different extension in the four models and mostly located in the central and eastern portions of the basin. O<sub>2</sub> decreases everywhere except for small areas around the equatorial upwelling band. The decrease is

very strong along the northern boundary of the Pacific Ocean and, depending on the model, at the subtropical gyre boundary (NorESM and, to a lesser extent, CanESM) and south of the Equator along the coast of Central and South America (IPSL).

In terms of variability, when comparing the two variables, very few areas in Fig. 11 have a comparable sign and amplitude (which would indicate comparable increases or decreases). IPV\* variability increases in the warm pool and to

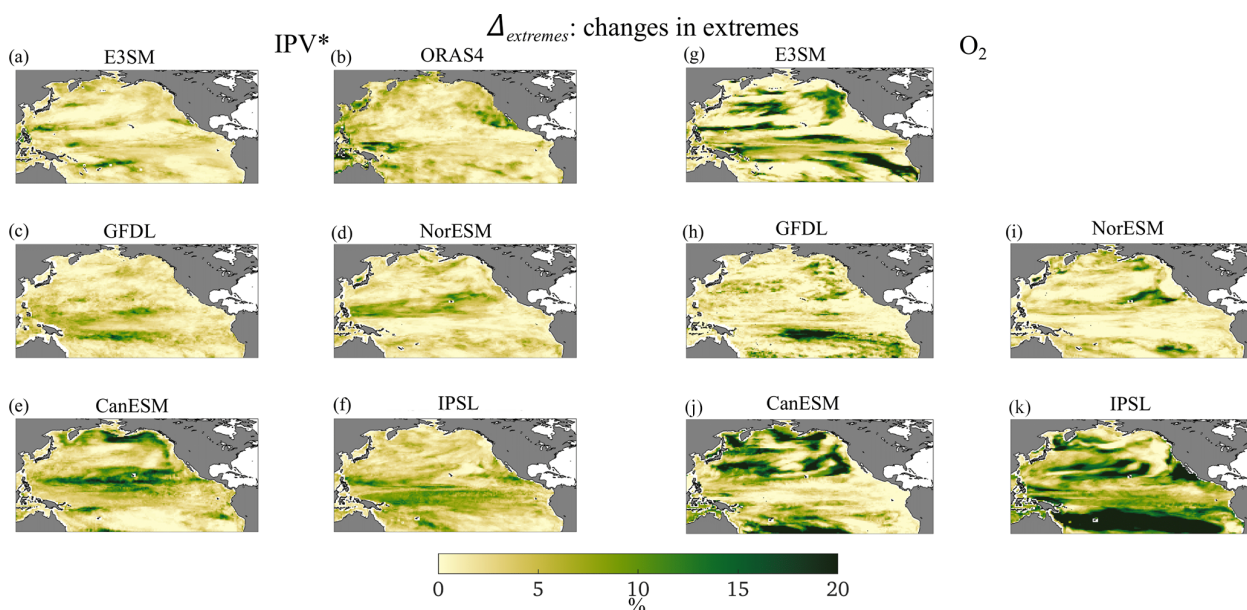


**Figure 8.** For the period from 1950 to 2014,  $\Delta_{\text{extremes}}$  for IPV\* (left) and  $O_2$  (right).

**Table 2.** Correlation coefficients (c.c.'s) for the period from 1950 to 2014 between the corresponding indicator maps for IPV\* and  $O_2$ . Bold values indicate a c.c.  $\geq 0.1$  that passed the shuffling significance test at the 5 % level (see Supplement). Numbers in parentheses reflect c.c.'s computed north of  $20^\circ$  N.

	E3SM-2G	GFDL	NorESM	CanESM	IPSL
$\Delta_{\text{means}}$ (means)	−0.01 (−0.02)	−0.07 (−0.07)	<b>−0.23 (−0.16)</b>	<b>−0.28 (−0.16)</b>	<b>−0.12 (−0.07)</b>
$\Delta_{\text{variability}}$ (variability)	<b>0.32 (0.24)</b>	<b>0.28 (0.23)</b>	0.04 (0.15)	<b>0.33 (0.21)</b>	<b>0.24 (0.18)</b>
$\Delta_{\text{extremes}}$ (extremes)	0.01 (−0.08)	<b>0.29 (0.05)</b>	<b>0.35 (0.47)</b>	0.09 (0.34)	−0.03 (0.17)

the south of the Equator in the eastern portion of the basin in all models except for NorESM.  $O_2$  variability increases in patchy areas mostly in the eastern half of the basin in GFDL, only along the southern boundary of the subtropical gyre in NorESM, roughly along the boundaries of the gyres in CanESM, and along the northern gyre boundary and south of the Equator in IPSL. Lastly, the extremes ( $\Delta_{\text{extremes}}$ ; Fig. 12) increase in CanESM and IPSL nearly everywhere except for the equatorial upwelling area for both variables, in NorESM in the Northern Hemisphere for  $O_2$  and in the ENSO region for IPV\*, and in GFDL along the northern boundary of the basin for IPV\* and in the northern and southern portions of the domain for  $O_2$ . Correlations among maps of the two variables are generally very small for all indicators in the projections (Table 3), with  $|c.c.| < 0.4$ , except for  $\Delta_{\text{means}}$  in NorESM and CanESM. Finally, we verified the robustness of our results to the choice of the ensemble member, computing the extreme indicators of four randomly chosen ensemble members of the CanESM model for the entire IPV\* and  $O_2$  signals during the historical periods. We found no significant changes in extremes and SED (Figs. S17–S18).

## 5 Discussion and conclusions

State-of-the-art Earth system models (ESMs) can simulate many aspects of the Earth's observed climate and biogeochemical processes, thereby offering valuable insights into the future. Challenges persist, however, in reliably representing ocean biogeochemical dynamics (Schartau et al., 2017; Fennel et al., 2022). Biogeochemical processes can involve intricate interactions between multiple components of the Earth system (Pascal et al., 2024). These processes are often nonlinear, and couplings with physical climate processes are complex and challenging to interpret (e.g., Béal et al., 2010), thus requiring advances in diagnostic methods and interpretation. To assess model performance, continued efforts to develop metrics for model evaluation are needed. In this study we present new tools stemming from data-mining techniques that may contribute to this end. These quantitative approaches, together with advances in observation-based gridded products, can better characterize and extract information about linkages between physical and biogeochemical variables. In particular, biogeochemical data, including dissolved oxygen measurements, remain sparsely available

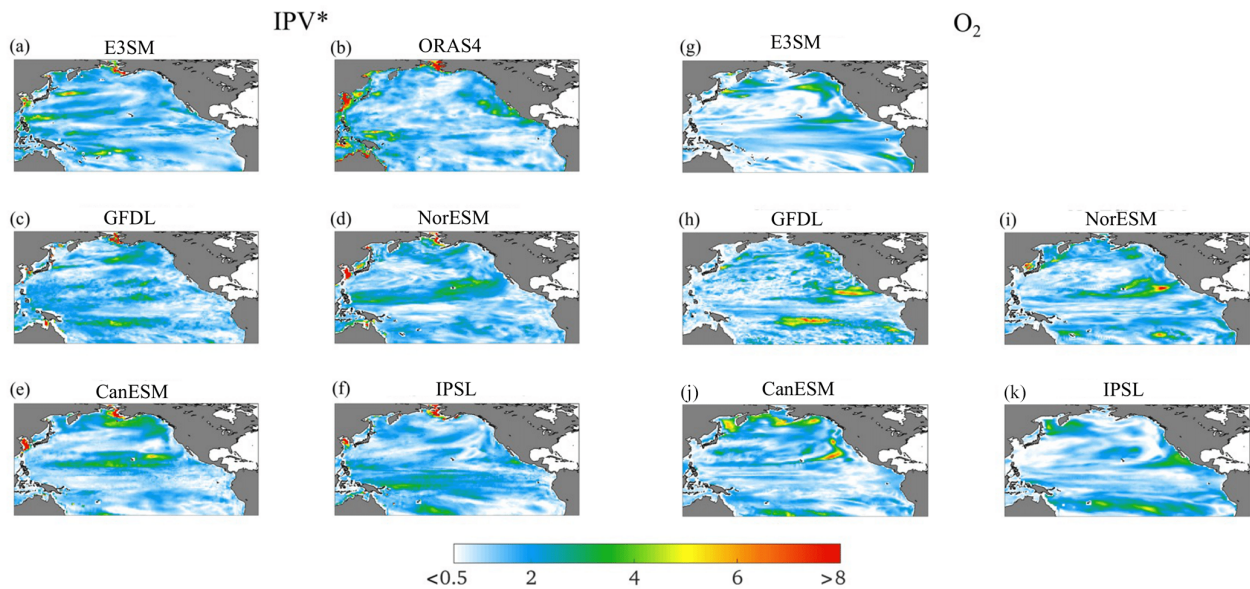


**Figure 9.** For the period from 1950 to 2014 (1960 to 2014 for E3SM-2G and ORAS4), SED index for IPV\* (left) and O<sub>2</sub> (right). The color scale is realized with rgmap (Greene, 2023).

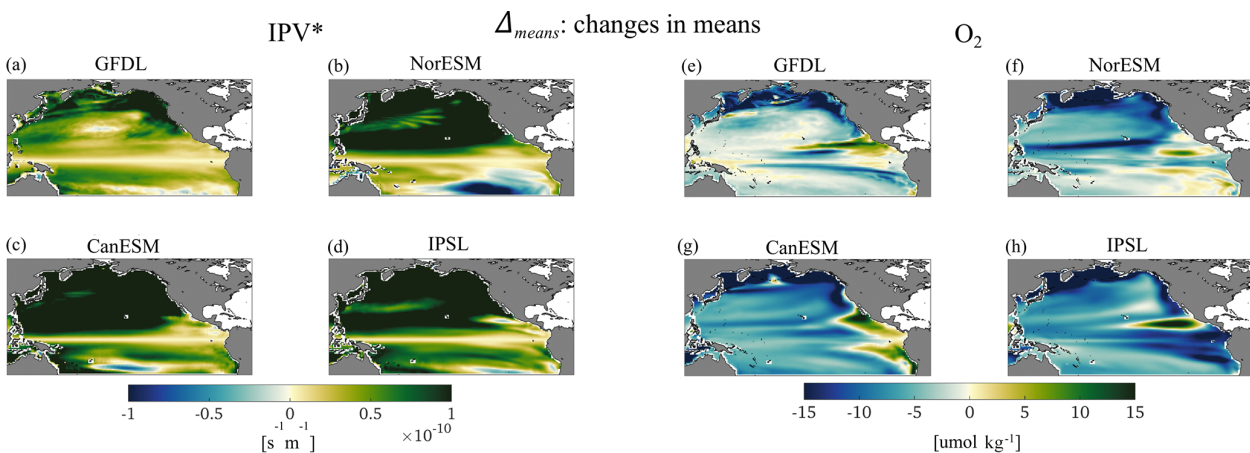


**Figure 10.** For the period from 2036 to 2100,  $\Delta_{means}$  for IPV\* (left) and O<sub>2</sub> (right).

compared to physical data. This limited availability of observational data hinders model validation. Exploiting linkages between the physical climate and oceanic O<sub>2</sub> can enhance the understanding and predictive skills of biogeochemical tracers. Examples of recently developed tools that take advantage of these linkages can be found in Giglio et al. (2018) and Sharp et al. (2023), who applied machine learning tools to the Argo-O<sub>2</sub> dataset to generate time-evolving maps of dissolved O<sub>2</sub> concentrations from seasonal to interannual timescales.

The overarching hypothesis in this work was that in the North Pacific, the spatiotemporal variability in O<sub>2</sub> reflects that of ocean ventilation (Talley et al., 2011), which can be measured by the magnitude of the isopycnic potential vorticity (IPV). A recent study (Ito et al., 2019) found that at sub-

tropical latitudes, the variability in wintertime mixed-layer depths and the subduction of O<sub>2</sub> are linked to the PDO. Elevated O<sub>2</sub> levels emerge downstream of the deepened winter mixed layer during the positive phase of the PDO. According to the same study, in the equatorial Pacific, the variability in upper-ocean O<sub>2</sub> is linked to the stratification and the depth of the thermocline, which in turn are modulated by the PDO. A wide range of mechanisms have been suggested for the connection between upper-ocean O<sub>2</sub> and ventilation, many of which can be represented in ESMs. We should note, however, that Ito et al. (2019) also showed that extratropical O<sub>2</sub> variability involves multiple types of physical–biogeochemical coupling that may compensate one another. For example, ventilation variability (Ridder and England, 2014; Duteil et



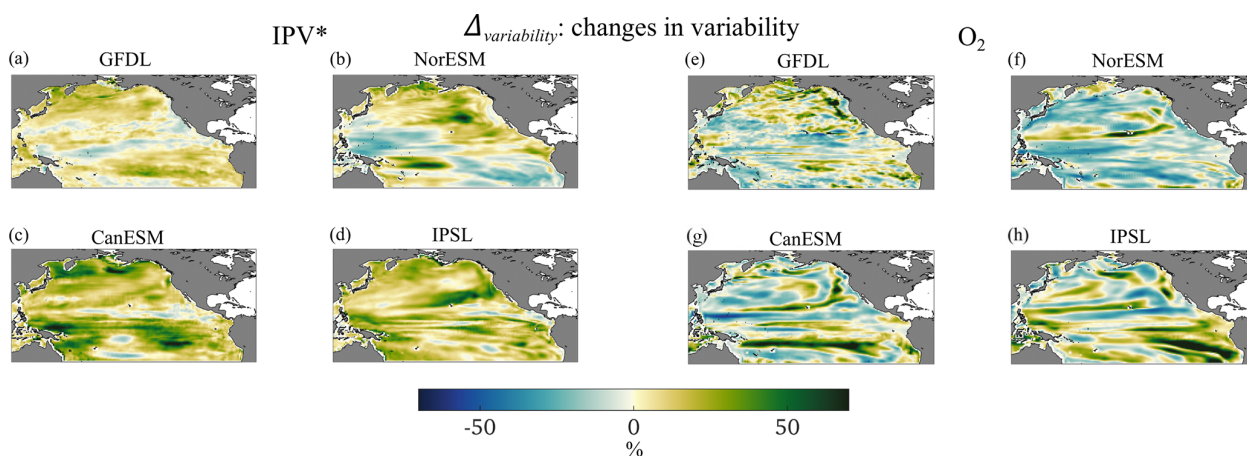


**Figure 11.** For the period from 2036 to 2100,  $\Delta_{\text{variability}}$  for IPV\* (left) and  $O_2$  (right).

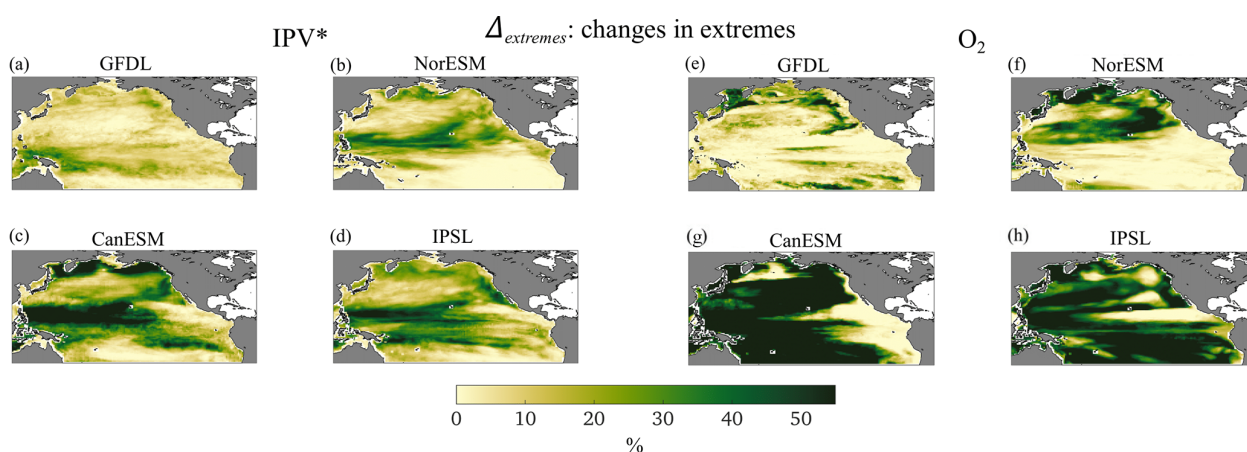


**Figure 12.** For the period from 2036 to 2100,  $\Delta_{\text{extremes}}$  for IPV\*<sub>res</sub> (left) and residual  $O_{2\text{res}}$  (right). The percentage shown reaches 60 % (3 times higher than during the historical period; Fig. 8).

al., 2014; McKinley et al., 2004) can have the opposite imprint on  $O_2$  than on water mass shifts, depending on the vertical stratification of temperature and  $O_2$ . In the subtropical thermocline, both temperature and  $O_2$  decrease with depth, and vertical shifts of water masses generate positive correlations between them (Brandt et al., 2015; Duteil et al., 2014; Eddebar et al., 2019). However, a negative relationship is expected between temperature and  $O_2$  under ventilation-driven variability, as colder conditions are typically associated with stronger ventilation (and thus higher  $O_2$ ). The superposition of these two processes may cause partial compensations and could amplify inter-model differences, especially in  $O_2$  concentrations.

In this work, we tested the overarching hypothesis that the  $O_2$  variability in the North Pacific is linked to that of ocean ventilation as measured by the magnitude of the isopycnic potential vorticity using four ESMs, a hindcast, and reanalysis data. We verified the simplistic view that the spatiotemporal variability in  $O_2$  reflects that of ocean ventilation through

the analysis of potential predictability, of the linkages between ventilation and  $O_2$  with the dominant climate modes of the North Pacific, and of the patterns of extreme events in ventilation and  $O_2$ . As a tracer of physical ventilation, we chose isopycnic potential vorticity or IPV\*. Strong ventilation is assumed to generate a negative anomaly in IPV\*, which is then advected and mixed by physical circulation and mixing processes. Ventilation supplies  $O_2$ -rich surface waters into the interior ocean, implying a negative correlation between  $O_2$  and IPV\*, as weak stratification (low IPV) may be linked to high oxygen. First, the information entropy (IE) was adopted to identify the areas in which IPV\* has a high predictability potential. Predictability was generally high along two stripes enclosing the ENSO pattern and excluding the upwelling cold tongue regions, which were found to correspond to areas in which  $O_2$  and IPV\* are strongly anticorrelated. The underlying mechanisms are relatively well understood (Ito et al., 2019), and this behavior is robust across all the analyzed datasets and does not change signifi-

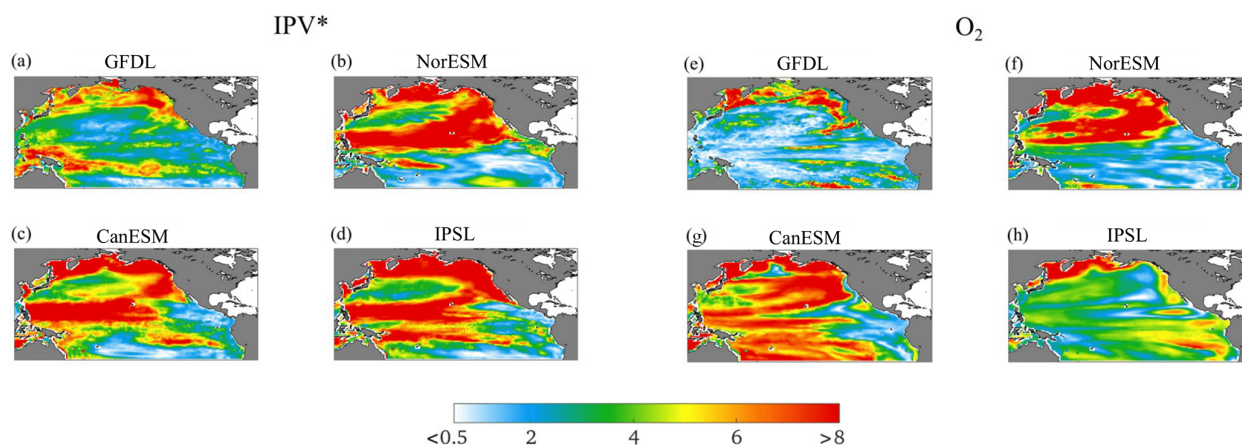


**Figure 13.** For the period from 2036 to 2100, SED index for IPV\* (left) and O<sub>2</sub> (right). The color scale was produced with rgbmap (Greene, 2023).

**Table 3.** The 2036–2100 correlation coefficients (c.c.'s) between the corresponding indicator maps for IPV\* and O<sub>2</sub>. Bold values indicate c.c.'s  $\geq 0.1$  that passed the shuffling significance test at the 5 % level (see Supplement). Numbers in parentheses reflect c.c.'s computed north of 20° N.

	GFDL-ESM4	NorESM2-LM	CanESM5	IPSL-CM6A-LR
$\Delta_{\text{means}}$	<b>-0.21 (-0.15)</b>	<b>-0.55 (-0.22)</b>	<b>-0.60 (-0.59)</b>	<b>-0.32 (-0.28)</b>
$\Delta_{\text{variability}}$	<b>0.30 (0.30)</b>	<b>0.14 (0.26)</b>	<b>0.21 (0.19)</b>	0.02 (0.00)
$\Delta_{\text{extremes}}$	-0.01 ( <b>0.56</b> )	<b>0.35 (0.40)</b>	<b>0.23 (0.01)</b>	0.08 (-0.02)

cantly in the future projections of the four ESMs. Therefore, around the Pacific Equator, IPV\*, which is easily retrievable from temperature and salinity data, has a good predictability potential (higher than in the rest of the basin) and can be used as a proxy for O<sub>2</sub>. The greater availability of temperature and salinity (and therefore stratification) observations from Argo floats, reanalyses, and modeled fields could be used in conjunction with the fewer co-located observations of O<sub>2</sub> to validate our findings and further extrapolate information about O<sub>2</sub> and its time evolution in these tropical areas.

Secondly, the variability in O<sub>2</sub> and IPV\* was examined in relation to large-scale modes of climate variability in the extratropical North Pacific. At mid-latitudes, the regional climate variability is PDO-dominated and our analysis shows very low predictability of IPV\*, unlike in the ENSO-dominated equatorial regions. The low predictability extends to the western boundary current and the Kuroshio–Oyashio Extension region. In the extratropical North Pacific, the (linear) contribution of the PDO to O<sub>2</sub> and IPV\* and the trends of their residuals have comparable amplitude over the historical period. This is not verified in the future projections, where the trends become increasingly dominant. Pattern correlations in the PDO regression maps (*b* coefficients) are generally quite small across the models.

Thirdly, we evaluated the hotspots of change in IPV\* and O<sub>2</sub> in the historical period and in the future projections. Overall, the historical hotspot indices or SED, computed sepa-

rately for IPV\* and O<sub>2</sub>, suggest a longitudinal decoupling across the two variables for all datasets except for one model, i.e., NorESM. In addition, most of the hotspots are in the extratropics. O<sub>2</sub> SEDs tend to be higher along the eastern portion of the basin, while IPV\* hotspots are mostly found over the western side of the basin and along the southern boundary of the subtropical gyre. The intensity of the SED increases over time from the historical period to the end of the 21st century. Larger changes and hotspots are found at the gyre boundaries and in the northern portion of the basin, from the Kamchatka Peninsula to the Gulf of Alaska. While O<sub>2</sub> loss is broadly linked to the strong increase in stratification, there are significant differences across model patterns, pointing to the need for further investigation.

The existing uncertainty in the CMIP6 models' representations of oxygen changes limits the information that can be extracted from the projections. We carried out our analysis on a sub-sample of the CMIP6 catalog only, but adding more models will not challenge this important conclusion. For a detailed model intercomparison of ocean deoxygenation in CMIP6 models, the reader is referred to Abe and Minobe (2023). Major sources of uncertainty in the future projections reside, for example, in their representation of the ENSO amplitude, as detailed in Beobide-Arsuaga et al. (2021), and in uncertainties regarding the amount of future warming (Tokarska et al., 2020) and, consequently, regarding the changes in upper-ocean stratification. Compared

to the CMIP5 catalog, CMIP6 models tend to warm more and show a decline in subsurface oxygen ventilation with no consistent decrease in inter-model uncertainties (Kwiatkowski et al., 2020). Here we found that while in some models the relationship between IPV\* and O<sub>2</sub> becomes stronger, that is not the case for all models, and it is not verified in GFDL, which has the highest horizontal resolution and best compares to the reanalyses in the historical period.

A note of caution should be spent on the representation of regional changes and hotspots. The currently available spatial resolution for CMIP6 models does not resolve the fine-scale (mesoscale and finer) physical and biogeochemical processes occurring near the coast. This is especially true in regions of elevated nutrient supply such as along the California Current System and, more generally, in the eastern boundary upwelling systems (EBUS). Consequently, projected oxygen trends may exhibit variability even within subregions under the same scenario, as shown for EBUS by Bograd et al. (2023). However, analysis at the scales required to capture coastal dynamics would require higher-resolution models that would need – if projected into the future – boundary conditions from CMIP6 simulations. CMIP6 models indeed remain the primary tool for evaluating changes in large-scale modes of climate variability at interannual to decadal timescales. While resolution is an important limitation for coastal areas, our main findings remain relevant to the interpretation of the large-scale forcing. In particular the outcome of the hotspot analysis, i.e., that there is a large-scale longitudinal decoupling between the areas of most prominent changes in IPV\* and O<sub>2</sub> despite the PDO imprinting, is unlikely to be influenced by the models' resolution.

We found that the linkages between extratropical O<sub>2</sub> and PDO are model dependent and that the relationship is not as strong as hypothesized on the basis of the sparse available observations. In summary, the variability across the current generation of CMIP models is, for some of our hypotheses, too large to reach any definite conclusion regarding a signal which is weaker than expected. To alleviate this problem, we suggest using the new BGC-Argo array to validate the performance of each model by testing relationships between temperature, IPV, and O<sub>2</sub>.

Models and reanalyses or hindcasts such as E3SM-2G allow for testing of whether there may be predictability, notwithstanding their biases and, for the case of the North Pacific, of whether there is a robust relationship across models between large-scale climate modes of variability, stratification, and O<sub>2</sub>. The predictability potential extrapolated by global ESMs represents an upper bound of the actual one, but it is useful for identifying when further exploration may be warranted or where such an exercise may simply be futile. For example, the information entropy could be evaluated using opportunely interpolated Argo data (e.g., Smith and Murphy, 2007; Cheng and Zhu, 2016; and for BGC-Argo, Turner et al., 2023; Keppler et al., 2023; Sharp et al., 2023). In regions where the predictability potential is high, such an ex-

ercise is warranted; wherever the potential predictability is low, it would be futile. In reference to our second hypothesis, we found that the PDO modulates IPV\* and O<sub>2</sub> but that the signal is not robust across models, thus limiting the possibility of reconstructing the large-scale evolution of O<sub>2</sub> from temperature and salinity data alone. On the other hand, in the equatorial regions generally undersampled in historical O<sub>2</sub> datasets, the relatively high predictability of IPV\* and its strong link to O<sub>2</sub> could be exploited.

In summary, in this work we examined the relationship between the upper-ocean (0–200 m) oxygen (O<sub>2</sub>) content and stratification in the North Pacific Ocean in four CMIP6 ESMs, an ocean hindcast simulation, and an ocean reanalysis. As far as the robustness of the relation between O<sub>2</sub> and IPV\* in the North Pacific is concerned (our first question), we found significant inter-model differences in the representation of climate variability in the North Pacific in CMIP6 models.

In relation to the linkages between O<sub>2</sub> and IPV\* compared to large-scale modes of climate variability such as PDO and ENSO (second question), we highlighted the potential of monitoring IPV\* to infer O<sub>2</sub> evolution in the ENSO area. However, we did not find a robust signal in terms of patterns and time evolution in the extratropics, where the PDO is the dominant mode of climate variability. The caveat is that the relationship, while weak, was nonetheless statistically significant under several metrics in the hindcast and in some models, of which GFDL-ESM4 is the best example.

Lastly, we found that the hotspots of changes in IPV\* and O<sub>2</sub> are not co-located (third and final question), which is especially true in the historical period.

In conclusion, the evolution trajectory of both stratification and oxygen in the North Pacific remains uncertain. Reducing this uncertainty would require monitoring IPV and O<sub>2</sub> simultaneously, for example through the accumulation of Argo floats equipped with CTD and O<sub>2</sub> sensors, to better quantify the large-scale co-variability in physical and biogeochemical parameters as a first step towards model improvement.

*Code and data availability.* The Python version of  $\delta$ -MAPS is available at <https://github.com/FabriFalasca/py-dMaps> (last access: 17 April 2024; <https://doi.org/10.5281/zenodo.7320415>, Falasca, 2022). The code for the information entropy computation is available at [https://github.com/FabriFalasca/NonLinear\\_TimeSeries\\_Analysis](https://github.com/FabriFalasca/NonLinear_TimeSeries_Analysis) (Falasca, 2020). Climate indices used in this study are from NOAA at <https://psl.noaa.gov/data/climateindices/list/> (PSL, 2024). The CMIP6 Earth system model output is available via the Earth System Grid Federation (<https://esgf-node.llnl.gov/search/cmip6/>, ESGF, 2022). The hotspot analysis was carried out using CDO (<https://doi.org/10.5281/zenodo.7112925>, Schulzweida, 2022). A sample code for the hotspot calculation is also available at <https://doi.org/10.5281/zenodo.13294399> (Ljuba, 2024). We used the *eof* Python package (Dawson, 2016) for EOF analysis of spatiotemporal data (available at <https://ajdawson.github.io/eofs/latest/api/eofs.standard.html>).

*Supplement.* The supplement related to this article is available online at: <https://doi.org/10.5194/bg-21-3985-2024-supplement>.

*Author contributions.* LN performed all analyses, AB and TI conceived the study, TI and YT helped to supervise the project, and YT led the E3SM-2G development and integration. AB took the lead in writing the manuscript. All authors provided critical feedback and helped to shape the research, analysis, and manuscript.

*Competing interests.* The contact author has declared that none of the authors have any competing interests.

*Disclaimer.* Publisher's note: Copernicus Publications remains neutral with regard to jurisdictional claims made in the text, published maps, institutional affiliations, or any other geographical representation in this paper. While Copernicus Publications makes every effort to include appropriate place names, the final responsibility lies with the authors.

*Acknowledgements.* We thank Fabrizio Falasca and Ilias Fountalis, who developed several of the software tools for the data-mining component of this project. We acknowledge the Gibbs SeaWater (GSW) Oceanographic Toolbox for Python (<https://teos-10.github.io/GSW-Python/intro.html>, last access: 17 April 2024; IOC, SCOR, and IAPSO, 2010; McDougall and Barker, 2011).

*Financial support.* The authors were supported by the Department of Energy, Regional and Global Model Analysis (RGMA) Program, grant no. 0000253789. Yohei Takano was supported by the U.S. Department of Energy, Office of Science, Office of Biological and Environmental Research, as part of the Energy Exascale Earth System Model project, and through a NERC–NSF grant (C-STREAMS, reference NE/W009579/1).

*Review statement.* This paper was edited by Ciavatta Stefano and reviewed by Pearse Buchanan and two anonymous referees.

## References

- Abe, Y. and Minobe, S.: Comparison of ocean deoxygenation between CMIP models and an observational dataset in the North Pacific from 1958 to 2005, *Front. Mar. Sci.*, 10, 1161451, <https://doi.org/10.3389/fmars.2023.1161451>, 2023.
- Balmaseda, M. A., Mogenssen, K., and Weaver, A. T.: Evaluation of the ECMWF ocean reanalysis system ORAS4, *Q. J. Roy. Meteor. Soc.*, 139, 1132–1161, <https://doi.org/10.1002/qj.2063>, 2012.
- Béal, D., Brasseur, P., Brankart, J.-M., Ourmières, Y., and Verron, J.: Characterization of mixing errors in a coupled physical biogeochemical model of the North Atlantic: implications for non-linear estimation using Gaussian anamorphosis, *Ocean Sci.*, 6, 247–262, <https://doi.org/10.5194/os-6-247-2010>, 2010.
- Beobide-Arsuaga, G., Bayr, T., Reintges, A., and Latif, M.: Uncertainty of ENSO-amplitude projections in CMIP5 and CMIP6 models, *Clim. Dynam.*, 56, 3875–3888, <https://doi.org/10.1007/s00382-021-05673-4>, 2021.
- Bindoff, N. L., Cheung, W. W. L., Kairo, J. G., Arístegui, J., Guinder, V. A., Hallberg, R., Hilmi, N., Jiao, N., Karim, M. D., Levin, L., O'Donoghue, S. H., Purca, S., Rinkevich, B., Suga, T., Tagliabue, A., Williamson, P.: *Changing Ocean, Marine Ecosystems, and Dependent Communities*, Cambridge, UK and New York, NY, USA, <https://doi.org/10.1017/9781009157964.007>, 2019.
- Bograd, S. J., Jacox, M., Hazen, E. L., Lovecchio, E., Montes, I., Pozo Buil, M., Shannon, L. J., Sydeman, W. J., and Rykaczewski, R. R.: Climate change impacts on eastern boundary upwelling systems, *Annu. Rev. Mar. Sci.*, 15, 303–328, 2023.
- Boucher, O., Servonnat, J., Albright, A. L., Aumont, O. Y. B., Bastriko, V., Bekki, S., Bonnet, R., Bony, S., Bopp, L., Brannonot, P., Brockmann, P., Cadule, P., Caubel, A., Cheru, F., Cozic, A., Cugnet, D., D'Andrea, F., Davini, P., de Lavergne, C., Denvil, S., Deshayes, J. M. D., Ducharme, A., Dufresne, J.-L., Dupont, E., Ethé, C., Fairhead, L., Falletti, L., Foujols, M.-A., Gardoll, S., Gastinea, G. J. G., Grandpeix, J.-Y., Guenet, B., Guez, L., Guilyardi, E., Guimberteau, M., Hauglustaine, D., Hourdin, F., Idelkadi, A., Joussaume, S., Kageyama, M., Khadre-Traoré, A., Khodri, M., Krinner, G., Lebas, N., Levvasseur, G., Lévy, C., Li, L., Lott, F., Lurton, T., Luysaert, S. G. M., Madeleine, J.-B., Maignan, F., Marchand, M., Marti, O., Mellul, L., Meurdesoif, Y., Mignot, J., Musat, I., Ottlé, C., Peylin, P., Planton, Y., Polcher, J., Rio, C., Rousset, C., Sepulchre, P., Sima, A., Swingedouw, D., Thieblemont, R., Traoré, A., Vancoppenolle, M., Vial, J., Vialard, J., Viovy, N., and Vuichard, N.: Presentation and evaluation of the IPSL-CM6A-LR climate model, *J. Adv. Model. Earth Syst.*, 12, e2019MS002010, <https://doi.org/10.1029/2019MS002010>, 2020.
- Box, G. E., Jenkins, G. M., and Reinsel, G. C.: *Time series analysis: forecasting and control*, Wiley, 2011.
- Brandt, P., Bange, H. W., Banyte, D., Dengler, M., Didwischus, S.-H., Fischer, T., Greatbatch, R. J., Hahn, J., Kanzow, T., Karstensen, J., Körtzinger, A., Krahnemann, G., Schmidtke, S., Stramma, L., Tanhua, T., and Visbeck, M.: On the role of circulation and mixing in the ventilation of oxygen minimum zones with a focus on the eastern tropical North Atlantic, *Biogeosciences*, 12, 489–512, <https://doi.org/10.5194/bg-12-489-2015>, 2015.
- Breitburg, D., Levin, L. A., Oschlies, A., Grégoire, M., Chavez, F. P., Conley, D. J., Garçon, V., Gilbert, D., Gutiérrez, D., Isensee, K., Jacinto, G. S., Limburg, K. E., Montes, I., Naqvi, S. W. A., Pitcher, G. C., Rabalais, N. N., Roman, M. R., Rose, K. A., Seibel, B. A., Telszewski, M., Yasuhara, M., and Zhang, J.: Declining oxygen in the global ocean and coastal waters, *Science*, 359, 46, <https://doi.org/10.1126/science.aam7240>, 2018.
- Burrows, S. M., Maltrud, M., Yang, X., Zhu, Q., Jeffery, N., Shi, X., Ricciuto, D., Wang, S., Bisht, G., Tang, J., Wolfe, J., Harrop, B. E., Singh, B., Brent, L., Baldwin, S., Zhou, T., Cameron-Smith, P., Keen, N., Collier, N., Xu, M., Hunke, E. C., Elliott, S. M., Turner, A. K., Li, H., Wang, H., Golaz, J.-C., Bond-Lamberty, B., Hoffman, F. M., Riley, W. J., Thornton, P. E., Calvin, K., and Leung, L. R.: The DOE E3SM v1.1 biogeochemistry configuration: Description and simulated ecosystem-climate responses to historical changes in forcing, *J. Adv. Model. Earth Sy.*, 12, e2019MS001766, <https://doi.org/10.1029/2019ms001766>, 2020.



- Cheng, L. and Zhu, J.: Benefits of CMIP5 Multimodel Ensemble in Reconstructing Historical Ocean Subsurface Temperature Variations, *J. Climate*, 29, 5393–5416, <https://doi.org/10.1175/JCLI-D-15-0730.1>, 2016.
- Christian, J. R., Denman, K. L., Hayashida, H., Holdsworth, A. M., Lee, W. G., Riche, O. G. J., Shao, A. E., Steiner, N., and Swart, N. C.: Ocean biogeochemistry in the Canadian Earth System Model version 5.0.3: CanESM5 and CanESM5-CanOE, *Geosci. Model Dev.*, 15, 4393–4424, <https://doi.org/10.5194/gmd-15-4393-2022>, 2022.
- Claret, M., Galbraith, E. D., Palter, J. B., Bianchi, D., Fennel, K., Gilbert, D., and Dunne, P. J.: Rapid coastal deoxygenation due to ocean circulation shift in the northwest Atlantic, *Nat. Clim. Change*, 8, 868–872, <https://doi.org/10.1038/s41558-018-0263-1>, 2018.
- Corso, G., Prado, T., Lima, G., Kurths, J., and Lopes, S.: Quantifying entropy using recurrence matrix microstates, *Chaos*, 28, 083108, <https://doi.org/10.1063/1.5042026>, 2018.
- Dawson, A.: eofs: A library for eof analysis of meteorological, oceanographic, and climate data, *Journal of Open Research Software*, 4, p. e14, <https://doi.org/10.5334/jors.122>, 2016 (code available at: <https://ajdawson.github.io/eofs/latest/api/eofs.standard.html>, last access: 17 April 2024).
- Deutsch, C., Ferrel, A., Seibel, B., Pörtner, H. O., and Huey, R. B.: Ecophysiology. Climate change tightens a metabolic constraint on marine habitats, *Science*, 348, 1132–1135, <https://doi.org/10.1126/science.aaa1605>, 2015.
- Diffenbaugh, N. S. and Giorgi, F.: Climate change hotspots in the CMIP5 global climate model ensemble, *Climatic Change*, 114, 813–822, 2012.
- Diffenbaugh, N. S., Giorgi, F., and Pal, J. S.: Climate change hotspots in the United States, *Geophys. Res. Lett.*, 35, L16709, <https://doi.org/10.1029/2008GL035075>, 2008.
- Dommengat, D. and Latif, M.: A cautionary note on the interpretation of EOFs, *J. Climate*, 15, 216–225, 2002.
- Dunne, J. P., Horowitz, L. W., Adcroft, A. J., Ginoux, P., Held, I. M., John, J. G., Krasting, J. P., Malyshev, S., Naik, V., Paulot, F., Shevliakova, E., Stock, C. A., Zadeh, N., Balaji, V., Blanton, C., Dunne, K. A., Dupuis, C., Durachta, J., Dussin, R., Gauthier, P. P. G., Griffies, S. M., Guo, H., Hallberg, R. W., Harrison, M., He, J., Hurlin, W., McHugh, C., Menzel, R., Milly, P. C. D., Nikonov, S., Paynter, D. J., Ploshay, J., Radhakrishnan, A., Rand, K., Reichl, B. G., Robinson, T., Schwarzkopf, D. M., Sentman, L. T., Underwood, S., Vahlenkamp, H., Winton, M., Wittenberg, A. T., Wyman, B., Zeng, Y., and Zhao, M.: The GFDL Earth System Model version 4.1 (GFDL-ESM 4.1): Overall coupled model description and simulation characteristics, *J. Adv. Model. Earth Sy.*, 12, e2019MS002015, <https://doi.org/10.1029/2019MS002015>, 2020.
- Duteil, O., Böning, C. W., and Oschlies, A.: Variability in subtropical-tropical cells drives oxygen levels in the tropical Pacific Ocean, *Geophys. Res. Lett.*, 41, 8926–8934, 2014.
- Eckmann, J. P., Kamphorst, S. O., and Ruelle, D.: Recurrence Plots of Dynamical Systems, *Europhys. Lett.*, 4, 973, <https://doi.org/10.1209/0295-5075/4/9/004>, 1987.
- Eddebar, Y. A., Rodgers, K. B., Long, M. C., Subramanian, A. C., Xie, S. P., and Keeling, R. F.: El Niño-like physical and biogeochemical ocean response to tropical eruptions, *J. Climate*, 32, 2627–2649, <https://doi.org/10.1175/JCLI-D-18-0458.1>, 2019.
- ESGF: WCRP Coupled Model Intercomparison Project (Phase 6), CMIP [data set], <https://esgf-node.llnl.gov/search/cmip6/> (last access: 17 April 2024), 2022.
- Eyring, V., Bony, S., Meehl, G. A., Senior, C. A., Stevens, B., Stouffer, R. J., and Taylor, K. E.: Overview of the Coupled Model Intercomparison Project Phase 6 (CMIP6) experimental design and organization, *Geosci. Model Dev.*, 9, 1937–1958, <https://doi.org/10.5194/gmd-9-1937-2016>, 2016.
- Falasca, F.: NonLinear\_TimeSeries\_Analysis, GitHub [code], [https://github.com/FabriFalasca/NonLinear\\_TimeSeries\\_Analysis](https://github.com/FabriFalasca/NonLinear_TimeSeries_Analysis) (last access: 17 April 2024), 2020.
- Falasca, F.: FabriFalasca/delta-MAPS: d-MAPS Java (v1.0), Zenodo [code], <https://doi.org/10.5281/zenodo.7320415>, 2022.
- Falasca, F. and Bracco, A.: Exploring the tropical Pacific manifold in models and observations, *Phys. Rev. X*, 12, 021054, <https://doi.org/10.1103/PhysRevX.12.021054>, 2022.
- Falasca, F., Bracco, A., Nenes, A., and Fountalis, I.: Dimensionality Reduction and Network Inference for Climate Data Using  $\delta$ -MAPS: Application to the CESM Large Ensemble Sea Surface Temperature, *J. Adv. Model. Earth Sy.*, 11, 1479–1515, <https://doi.org/10.1029/2019MS001654>, 2019.
- Falasca, F., Crétat, J., Braconnot, P., and Bracco, A.: Spatiotemporal complexity and time-dependent networks in sea surface temperature from mid- to late Holocene, *Eur. Phys. J. Plus*, 135, 392, <https://doi.org/10.1140/epjp/s13360-020-00403-x>, 2020.
- Fennel, K., Mattern, J. P., Doney, S. C., Laurent Bopp, L., Moore, A. M., Wang, B., and Yu, L.: Ocean biogeochemical modelling, *Nature Reviews Methods Primers*, 2, 76, <https://doi.org/10.1038/s43586-022-00154-2>, 2022.
- Fountalis, I., Dovrolis, C., Bracco, A., Dilkina, B., and Keilholz, S.:  $\delta$ -MAPS: from spatio-temporal data to a weighted and lagged network between functional domains, *Appl. Netw. Sci.*, 3, 21, <https://doi.org/10.1007/s41109-018-0078-z>, 2018.
- Garcia, H. E., Boyer, T. P., Baranova, O. K., Locarnini, R. A., Mishonov, A. V., Grodsky, A., Paver, C. R., Weathers, K. W., Smolyar, I. V., Reagan, J. R., Seidov, D., and Zweng, M. M.: World ocean atlas 2018: Product documentation, A. Mishonov, Technical Editor, 2019.
- Giglio, D., Lyubchich, V., and Mazloff, M. R.: Estimating Oxygen in the Southern Ocean Using Argo Temperature and Salinity, *J. Geophys. Res.-Oceans*, 123, 4280–4297, 2018.
- Gnanadesikan, A., Dunne, J. P., and John, J.: Understanding why the volume of suboxic waters does not increase over centuries of global warming in an Earth System Model, *Biogeosciences*, 9, 1159–1172, <https://doi.org/10.5194/bg-9-1159-2012>, 2012.
- Gnanadesikan, A., Bianchi, D., and Pradal, M. A.: Critical role for mesoscale eddy diffusion in supplying oxygen to hypoxic ocean waters, *Geophys. Res. Lett.*, 40, 5194–5198, <https://doi.org/10.1002/GRL.50998>, 2013.
- Gnanadesikan, A., Pradal, M., and Abernathey, R.: Isopycnal mixing by mesoscale eddies significantly impacts oceanic anthropogenic carbon uptake, *Geophys. Res. Lett.*, 42, 4249–4255, <https://doi.org/10.1002/2015GL064100>, 2015.
- Golaz, J.-C., Van Roekel, L. P., Zheng, X., Roberts, A. F., Wolfe, J. D., Lin, W., Bradley, A. M., Tang, Q., Maltrud, M. E., Forsyth, R. M., Zhang, C., Zhou, T., Zhang, K., Zender, C. S., Wu, M., Wang, H., Turner, A. K., Singh, B., Richter, J. H., Qin, Y., Petersen, M. R., Marnett, A., Ma, P.-L., Larson, V. E., Krishna, J., Keen, N. D., Jeffery, N., Hunke, E. C., Hannah, W. M., Guba,

- O., Griffin, B. M., Feng, Y., Engwirda, D., Di Vittorio, A. V., Dang, C., Conlon, L. M., Chen, C.-C.-J., Brunke, M. A., Bisht, G., Benedict, J. J., Asay-Davis, X. S., Zhang, Y., Zhang, M., Zeng, X., Xie, S., Wolfram, P. J., Vo, T., Veneziani, M., Tesfa, T. K., Sreepathi, S., Salinger, A. G., Reeves Eyre, J. E. J., Prather, M. J., Mahajan, S., Li, Q., Jones, P. W., Jacob, R. L., Huebler, G. W., Huang, X., Hillman, B. R., Harrop, B. E., Foucar, J. G., Fang, Y., Comeau, D. S., Caldwell, P. M., Bartoletti, T., Balaguru, K., Taylor, M. A., McCoy, R. B., Leung, L. R., and Bader, D. C.: The DOE E3SM Model Version 2: overview of the physical model and initial model evaluation, *J. Adv. Model. Earth Sy.*, 14, e2022MS003156, <https://doi.org/10.1029/2022ms003156>, 2022.
- Gordon, E. M., Barnes, E. A., and Hurrell, J. W.: Oceanic harbingers of Pacific Decadal Oscillation predictability in CESM2 detected by neural networks, *Geophys. Res. Lett.*, 48, e2021GL095392, <https://doi.org/10.1029/2021GL095392>, 2021.
- Greene, C.: rgbmap color maps, MATLAB Central File Exchange, <https://www.mathworks.com/matlabcentral/fileexchange/46874-rgbmap-color-maps>, last access: 27 June 2023.
- Kuyajolu, O. J., Falasca, F., and Bracco, A.: Information Entropy as Quantifier of Potential Predictability in the Tropical Indo-Pacific Basin, *Front. Clim.*, 3, 675840, <https://doi.org/10.3389/fclim.2021.675840>, 2021.
- IOC, SCOR and IAPSO: The international thermodynamic equation of seawater – 2010: Calculation and use of thermodynamic properties. Intergovernmental Oceanographic Commission, Manuals and Guides No. 56, UNESCO, 196 pp., 2010.
- Ito, T., Minobe, S., Long, M. C., and Deutsch, C.: Upper ocean O<sub>2</sub> trend: 1958–2015, *Geophys. Res. Lett.*, 44, 4214–4223, <https://doi.org/10.1002/2017GL073613>, 2017.
- Ito, T., Long, M. C., Deutsch, C., Minobe, S., and Sun, D.: Mechanisms of low-frequency oxygen variability in the North Pacific, *Global Biogeochem. Cy.*, 33, 110–124, <https://doi.org/10.1029/2018GB005987>, 2019.
- Keppler, L., Landschützer, P., Lauvset, S. K., and Gruber, N.: Recent trends and variability in the oceanic storage of dissolved inorganic carbon, *Global Biogeochem. Cy.*, 37, e2022GB007677, <https://doi.org/10.1029/2022GB007677>, 2023.
- Kucharski, F., Bracco, A., Yoo, J. H., and Molteni, F.: Atlantic forced component of the Indian monsoon interannual variability, *Geophys. Res. Lett.*, 35, L04706, <https://doi.org/10.1029/2007gl033037>, 2008.
- Kwiatkowski, L., Torres, O., Bopp, L., Aumont, O., Chamberlain, M., Christian, J. R., Dunne, J. P., Gehlen, M., Ilyina, T., John, J. G., Lenton, A., Li, H., Lovenduski, N. S., Orr, J. C., Palmieri, J., Santana-Falcón, Y., Schwinger, J., Séférian, R., Stock, C. A., Tagliabue, A., Takano, Y., Tjiputra, J., Toyama, K., Tsujino, H., Watanabe, M., Yamamoto, A., Yool, A., and Ziehn, T.: Twenty-first century ocean warming, acidification, deoxygenation, and upper-ocean nutrient and primary production decline from CMIP6 model projections, *Biogeosciences*, 17, 3439–3470, <https://doi.org/10.5194/bg-17-3439-2020>, 2020.
- Li, S., Wu, L., Yang, Y., Geng, T., Cai, W., Gan, B., Chen, Z., Jing, Z., Wang, G., and Ma, X.: The Pacific Decadal Oscillation less predictable under greenhouse warming, *Nat. Clim. Change*, 10, 30–34, <https://doi.org/10.1038/s41558-019-0663-x>, 2020.
- Ljuba, N.: superlju/IPVO2hotspots: v1.0.0 (v1.0.0), Zenodo [code], <https://doi.org/10.5281/zenodo.13294400>, 2024.
- Long, M. C., Moore, J. K., Lindsay, K., Levy, M., Doney, S. C., Luo, J. Y., Krumhardt, K. M., Letscher, R. T., Grover, M., and Sylvester, Z. T.: Simulations With the Marine Biogeochemistry Library (MARBL), *J. Adv. Model. Earth Sy.*, 13, e2021MS002647, <https://doi.org/10.1029/2021MS002647>, 2021.
- Mantua, N. J., Hare, S. R., Zhang, Y., Wallace, J. M., and Francis, R. C.: A Pacific interdecadal climate oscillation with impacts on salmon production, *B. Am. Meteorol. Soc.*, 78, 1069–1080, 1997.
- Marwan, N., Romano, M. C., Thiel, M., and Kurths, J.: Recurrence plots for the analysis of complex systems, *Phys. Rep.*, 438, 237–329, <https://doi.org/10.1016/j.physrep.2006.11.001>, 2007.
- McDougall, T. J. and Barker, P. M.: Getting started with TEOS-10 and the Gibbs Seawater (GSW) Oceanographic Toolbox, 28 pp., SCOR/IAPSO WG127, ISBN 978-0-646-55621-5, 2011.
- McKinley, G. A., Follows, M. J., and Marshall, J.: Mechanisms of air-sea CO<sub>2</sub> flux variability in the equatorial Pacific and the North Atlantic, *Global Biogeochem. Cy.*, 18, C07S06, <https://doi.org/10.1029/2003GB002179>, 2004.
- Mogensen, K., Balmaseda, M. A., and Weaver, A.: The NEMOVAR ocean data assimilation system as implemented in the ECMWF ocean analysis for System 4, ECMWF Technical Memorandum, 668, 1–59, <https://doi.org/10.21957/x5y9yrtm>, 2012.
- Nevison, C., Butler, J. H., and Elkins, J. W.: Global distribution of N<sub>2</sub>O and the ΔN<sub>2</sub>O-AOU yield in the subsurface ocean, *Global Biogeochem. Cy.*, 17, 1119, <https://doi.org/10.1029/2003GB002068>, 2003.
- Pascal, L., Cool, J., Archambault, P., Calosi, P., Cuenca, A. L. R., Mucci, A. O., and Chaillou, G.: Ocean deoxygenation caused non-linear responses in the structure and functioning of benthic ecosystems, *Glob. Change Biol.*, e16994, <https://doi.org/10.1111/gcb.16994>, 2024.
- Prado, T., Corso, G., Santos Lima, G., Budzinski, R., Boaretto, B., Ferrari, F., Macau, E. E. N., and Lopes, S. R.: Maximum entropy principle in recurrence plot analysis on stochastic and chaotic systems, *Chaos*, 30, 043123, <https://doi.org/10.1063/1.5125921>, 2020.
- PSL: Climate Indices: Monthly Atmospheric and Ocean Time Series, Physical Sciences Laboratory, <https://psl.noaa.gov/data/climateindices/list/>, last access: 17 April 2024.
- Redi, M. H.: Oceanic Isopycnal Mixing by Coordinate Rotation, *J. Phys. Oceanogr.*, 12, 1154–1158, 1982.
- Ridder, N. N. and England, M. H.: Sensitivity of ocean oxygenation to variations in tropical zonal wind stress magnitude, *Global Biogeochem. Cy.*, 28, 909–926, 2014.
- Roemmich, D., Alford, M. H., Claustre, H., Johnson, K., King, B., Moum, J., Oke, P., Owens, W. B., Pouliquen, S., Purkey, S., Scanderbeg, M., Suga, T., Wijffels, S., Zilberman, N., Bakker, D., Baringer, M., Belbeoch, M., Bittig, H. C., Boss, E., Calil, P., Carse, F., Carval, T., Chai, F., Conchubhair, D. Ó., d'Ortenzio, F., Dall'Olmo, G., Desbruyeres, D., Fennel, K., Fer, I., Ferrari, R., Forget, G., Freeland, H., Fujiki, T., Gehlen, M., Greenan, B., Hallberg, R., Hibiya, T., Hosoda, S., Jayne, S., Jochum, M., Johnson, G. C., Kang, K., Kolodziejczyk, N., Körtzinger, A., Traon, P.-Y. L., Lenn, Y.-D., Maze, G., Mork, K. A., Morris, T., Nagai, T., Nash, J., Garabato, A. N., Olsen, A., Patabhi, R. R., Prakash, S., Riser, S., Schmechtig, C., Schmid, C., Shroyer, E., Sterl, A., Sutton, P., Talley, L., Tanhua, T., Thierry,

- V., Thomalla, S., Toole, J., Troisi, A., Trull, T. W., Turton, J., Velez-Belchi, P. J., Walczowski, W., Wang, H., Wanninkhof, R., Waterhouse, A. F., Waterman, S., Watson, A., Wilson, C., Wong, A. P. S., Xu, J., and Yasuda, I.: On the future of Argo: A global, full-depth, multi-disciplinary array, *Front. Mar. Sci.*, 6, 439, <https://doi.org/10.3389/fmars.2019.00439>, 2019.
- Rudnickas Jr., D., Palter, J., Hebert, D., and Rossby, H. T.: Isopycnal mixing in the North Atlantic oxygen minimum zone revealed by RAFOS floats, *J. Geophys. Res.-Oceans*, 124, 6478–6497, <https://doi.org/10.1029/2019JC015148>, 2019.
- Sallée, J. B., Rintoul, S. R., and Wijffels, S. E.: Southern ocean thermocline ventilation, *J. Phys. Oceanogr.*, 40, 509–529, 2010.
- Sallée, J.-B., Matear, R. J., Rintoul, S. R., and Lenton, A.: Localized subduction of anthropogenic carbon dioxide in the Southern Hemisphere oceans, *Nat. Geosci.*, 5, 579–584, <https://doi.org/10.1038/ngeo1523>, 2012.
- Schartau, M., Wallhead, P., Hemmings, J., Löptien, U., Kriest, I., Krishna, S., Ward, B. A., Slawig, T., and Oschlies, A.: Reviews and syntheses: parameter identification in marine planktonic ecosystem modelling, *Biogeosciences*, 14, 1647–1701, <https://doi.org/10.5194/bg-14-1647-2017>, 2017.
- Schulzweida, U.: CDO User Guide (2.1.0), Zenodo [code], <https://doi.org/10.5281/zenodo.7112925>, 2022.
- Schmidtko, S., Stramma, L., and Visbeck, M.: Decline in global oceanic oxygen content during the past five decades, *Nature*, 542, 335–339, <https://doi.org/10.1038/nature21399>, 2017.
- Seland, Ø., Bentsen, M., Olivé, D., Toniazzo, T., Gjermundsen, A., Graff, L. S., Debernard, J. B., Gupta, A. K., He, Y.-C., Kirkevåg, A., Schwinger, J., Tjiputra, J., Aas, K. S., Bethke, I., Fan, Y., Griesfeller, J., Grini, A., Guo, C., Ilicak, M., Karset, I. H. H., Landgren, O., Liakka, J., Moseid, K. O., Nummelin, A., Spensberger, C., Tang, H., Zhang, Z., Heinze, C., Iversen, T., and Schulz, M.: Overview of the Norwegian Earth System Model (NorESM2) and key climate response of CMIP6 DECK, historical, and scenario simulations, *Geosci. Model Dev.*, 13, 6165–6200, <https://doi.org/10.5194/gmd-13-6165-2020>, 2020.
- Sharp, J. D., Fassbender, A. J., Carter, B. R., Johnson, G. C., Schultz, C., and Dunne, J. P.: GOBAI-O2: temporally and spatially resolved fields of ocean interior dissolved oxygen over nearly 2 decades, *Earth Syst. Sci. Data*, 15, 4481–4518, <https://doi.org/10.5194/essd-15-4481-2023>, 2023.
- Smith, D. M. and Murphy, J. M.: An objective ocean temperature and salinity analysis using covariances from a global climate model, *J. Geophys. Res.-Oceans*, 112, C02022, <https://doi.org/10.1029/2005JC003172>, 2007.
- Stock, C. A., Dunne, J. P., Fan, S., Ginoux, P., John, J., Krasting, J. P., Laufkötter, C., Paulot, F., and Zadeh, N.: Ocean Biogeochemistry in GFDL's Earth System Model 4.1 and Its Response to Increasing Atmospheric CO<sub>2</sub>, *J. Adv. Model. Earth Sy.*, 12, e2019MS002043, <https://doi.org/10.1029/2019MS002043>, 2020.
- Swart, N. C., Cole, J. N. S., Kharin, V. V., Lazare, M., Scinocca, J. F., Gillett, N. P., Anstey, J., Arora, V., Christian, J. R., Hanna, S., Jiao, Y., Lee, W. G., Majaess, F., Saenko, O. A., Seiler, C., Seinen, C., Shao, A., Sigmond, M., Solheim, L., von Salzen, K., Yang, D., and Winter, B.: The Canadian Earth System Model version 5 (CanESM5.0.3), *Geosci. Model Dev.*, 12, 4823–4873, <https://doi.org/10.5194/gmd-12-4823-2019>, 2019.
- Takano, Y., Maltrud, M., Sinha, A., Jeffery, N., Smith, K., Conlon, L., Wolfe, J., and Petersen, M.: Global Ocean Carbon Cycle Simulations with the 2 E3SM version 2 (E3SMv2), Zenodo, <https://doi.org/10.5281/zenodo.10093369>, 2023.
- Talley, L. D., Pickard, G. L., Emery, W. J., and Swift, J. H.: Descriptive Physical Oceanography: An Introduction, 6th Edn., Academic Press, Elsevier Ltd., New York, 983 pp., 2011.
- Tjiputra, J. F., Schwinger, J., Bentsen, M., Morée, A. L., Gao, S., Bethke, I., Heinze, C., Goris, N., Gupta, A., He, Y.-C., Olivé, D., Seland, Ø., and Schulz, M.: Ocean biogeochemistry in the Norwegian Earth System Model version 2 (NorESM2), *Geosci. Model Dev.*, 13, 2393–2431, <https://doi.org/10.5194/gmd-13-2393-2020>, 2020.
- Tokarska, K. B., Stolpe, M. B., Sippel, S., Fischer, E. M., Smith, C. J., Lehner, F., and Knutti, R.: Past warming trend constrains future warming in CMIP6 models, *Sci. Adv.*, 6, eaaz9549, <https://doi.org/10.1126/sciadv.aaz9549>, 2020.
- Turco, M., Palazzi, E., Hardenberg, J., and Provenzale, A.: Observed climate change hotspots, *Geophys. Res. Lett.*, 42, 3521–3528, 2015.
- Tsujino, H., Urakawa, L. S., Griffies, S. M., Danabasoglu, G., Adcroft, A. J., Amaral, A. E., Arsouzé, T., Bentsen, M., Bernardello, R., Böning, C. W., Bozec, A., Chassignet, E. P., Danilov, S., Dussin, R., Exarchou, E., Fogli, P. G., Fox-Kemper, B., Guo, C., Ilicak, M., Iovino, D., Kim, W. M., Koldunov, N., Lapin, V., Li, Y., Lin, P., Lindsay, K., Liu, H., Long, M. C., Komuro, Y., Marsland, S. J., Masina, S., Nummelin, A., Rieck, J. K., Ruprich-Robert, Y., Scheinert, M., Sicardi, V., Sidorenko, D., Suzuki, T., Tatebe, H., Wang, Q., Yeager, S. G., and Yu, Z.: Evaluation of global ocean–sea-ice model simulations based on the experimental protocols of the Ocean Model Intercomparison Project phase 2 (OMIP-2), *Geosci. Model Dev.*, 13, 3643–3708, <https://doi.org/10.5194/gmd-13-3643-2020>, 2020.
- Turner, K. E., Smith, D. M., Katavouta, A., and Williams, R. G.: Reconstructing ocean carbon storage with CMIP6 Earth system models and synthetic Argo observations, *Biogeosciences*, 20, 1671–1690, <https://doi.org/10.5194/bg-20-1671-2023>, 2023.
- Williams, J. W., Jackson, S. T., and Kutzbach, J. E.: Projected distributions of novel and disappearing climates by 2100 AD, *P. Natl. Acad. Sci. USA*, 104, 5738–5742, 2007.
- Yang, S., Gruber, N., Long, M. C., and Vogt, M.: ENSO-driven variability of denitrification, *Global Biogeochem. Cy.*, 31, 1470–1487, <https://doi.org/10.1002/2016gb005596>, 2017.